

Crustal-scale fluid circulation and co-seismic shallow comb-veining along the longest normal fault of the central Apennines, Italy

Luca Smeraglia ^a, Stefano M. Bernasconi ^b, Fabrizio Berra ^c, Andrea Billi ^d, Chiara Boschi ^e, Antonio Caracausi ^f, Eugenio Carminati ^{a,d}, Francesca Castorina ^{a,d}, Carlo Doglioni ^{a,g}, Francesco Italiano ^f, Andrea Luca Rizzo ^f, I. Tonguç Uysal ^{h,i}, Jian-xin Zhao ^j

^a Dipartimento di Scienze della Terra, Sapienza Università di Roma, P.le Aldo Moro 5, 00185, Roma, Italy

^b Geological Institute, ETH Zürich, Sonneggstrasse 5, 8092 Zürich, Switzerland

^c Dipartimento di Scienze della Terra, Università degli Studi di Milano, Via Mangiagalli 34, 20133 Milano, Italy

^d Consiglio Nazionale delle Ricerche c.o. Dipartimento di Scienze della Terra, Sapienza Università di Roma, P.le Aldo Moro 5, 00185 Roma, Italy

^e Istituto di Geoscienze e Georisorse, Consiglio Nazionale delle Ricerche, Via Moruzzi 1, 56124 Pisa, Italy

^f Istituto Nazionale di Geofisica e Vulcanologia, Sezione di Palermo, Via Ugo La Malfa 153, 90146 Palermo, Italy

^g Istituto Nazionale di Geofisica e Vulcanologia, sede di Roma, Via di Vigna Murata 605, 00143 Roma, Italy

^h CSIRO Energy, 26 Dick Perry Avenue, Kensington, WA 6151, Australia

ⁱ Queensland Geothermal Energy Centre of Excellence, The University of Queensland, Queensland 4072, Australia

^j Radiogenic Isotope Facility, School of Earth Sciences, The University of Queensland, Brisbane, Qld 4072, Australia

ABSTRACT

The extensional Val Roveto Fault, which is the longest exhumed potentially-seismogenic structure of central Apennines, Italy, is examined to constrain earthquake-related fluid circulation and fluid sources within shallow carbonate-hosted faults. The study focuses on fault-related comb and slip-parallel veins that are calcite-filled and cut through the principal surface of the Val Roveto Fault. We observe multiple crack-and-seal events characterized by several veining episodes, probably related to different slip increments along the fault plane. We show that vein calcite precipitated in Late Pleistocene time below the present-day outcrop level at a maximum depth of ~350 m and temperatures between 32 and 64 °C from meteoric-derived fluids modified by reactions with crustal rocks and with a mantle contribution (up to ~39%). The observed warm temperatures are not compatible with a shallow (\leq ~350 m) precipitation depth, which, in this region, is dominated by circulation of cold meteoric water and/or shallow groundwater. Based on structural-geochemical data, we propose that deep-seated crust-mantle-derived warm fluids were squeezed upward during earthquakes and were hence responsible for calcite precipitation at shallow depths in co-seismic comb and slip-parallel fractures. As comb- and slip-parallel veins are rather common, particularly along seismogenic extensional faults, we suggest that further studies are necessary to test whether these veins are often of co-seismic origin. If so, they may become a unique and irreplaceable tool to unravel the seismic history of hazardous active faults.

Keywords: comb fractures calcite veins fault–fluid interaction fluid inclusions carbonate faults seismicity

1. Introduction

Faults and fault zones can modulate fluid circulation within the brittle upper crust acting as barriers or conduits for the passage of fluids such as groundwater, hydrothermal waters, and hydrocarbons. Fluids, in particular, can be mobilized during earthquakes as well as during the entire seismic cycle as testified by seismological (e.g., the V_p/V_s ratio changes during the 2009, M_w 6.3, L'Aquila earthquake; Malagnini et al., 2012) and hydrogeochemical (e.g., input of deep metal-rich fluids into shallow aquifers during the 2016 Amatrice-Norcia earthquakes; Barberio et al., 2017) studies. Accordingly, veins along faults can be the record of dynamic dilation and fracture opening during seismic events (Boullier et al., 2004; Williams et al., 2017). Such dynamic fluid mobilization, in particular, allows fluid re-distribution and mixing from different reservoirs (i.e., mantle, crustal, meteoric; Menzies et al., 2014; Barberio et al., 2017).

Geochemical tracers (e.g., REE-pattern, isotopes, fluid inclusions) within fault-related veins can therefore be used to infer the timing and pathways of fluids circulating within the crust in relation with the seismic cycles (Uysal et al., 2011; Ünal-Imer et al., 2016). Fault-related fluid circulation is indeed ruled by several parameters such as fault rock porosity and permeability, but also by the spatio-temporal evolution of fault-related permeability (Evans et al., 1997; Balsamo et al., 2016) including the seismic cycle-controlled permeability (Sibson, 2000). For these reasons, the study of fault-related veins is fundamental to better understand and build models of fluid circulation within the Earth's crust, also in association with past earthquakes and seismic cycles.

In this paper, we examine three exposures located along the southeastern sector of the Val Roveto Fault (VRF, Fig. 1), a major carbonate/clay-hosted extensional fault exhumed from depths <3 km within the seismically active carbonate domain of the central Apennines, Italy. The VRF is the longest (i.e., ~60 km-long) potentially-seismogenic extensional fault in the central Apennines and exhibits excellent fault exposures for studying fault–fluid interactions and earthquake-related fluid circulation within an active extensional tectonic setting. We combine structural and microstructural analyses with various geochemical

methods to constrain multiple events of earthquake-related fracturing and mineralization as well as the origin of circulating fluids during coseismic to early post-seismic times. We conclude that normal fault-related earthquakes can promote crustal-scale fluid circulation and extensional faults can provide preferential pathways for the rapid ascent of crustal fluids with mantle contribution and allow their mixing with meteoric water and/or groundwater at shallow levels.

2. Geological setting 2.1. Central Apennines

The Apennines are a NW-SE-oriented fold-thrust belt generated by the eastward roll-back of the Adriatic plate below the European plate (Carminati et al., 2012). Shortening has been mainly accommodated by NW-SE-oriented thrust faults, which scraped off and juxtaposed the pre-orogenic sedimentary sequence of the Adriatic plate above the syn-orogenic sedimentary deposits (Mostardini and Merlini, 1986; Fig. 1). In particular, the pre-orogenic sedimentary sequence consists of ~4,000–5,000 m-thick Upper Triassic–Middle Miocene carbonates deposited in shallow-water carbonate platform and ramp environments above the underlying crystalline basement of the Adriatic plate (Cosentino et al., 2010; Fig. 1). These deposits are overlain by Upper Miocene–Messinian syn-orogenic deposits consisting of up to ~100 m-thick hemipelagic marls and up to ~3,000 m-thick siliciclastic sandstones with marly and clayey interbeds deposited within foreland and foredeep environments, respectively (Cosentino et al., 2010; Fig. 1). This sedimentary succession is vertically duplicated or even triplicated due to orogenic shortening.

Since the Early Pliocene, the internal and axial part of the central Apennines has undergone post-orogenic exhumation and extension associated with the development of the Tyrrhenian backarc basin. This extensional regime has generated a system of NW-SE-oriented extensional faults (Cavatino and De Celles, 1999; Fig. 1), which have dissected the fold-thrust belt and generated historically- and instrumentally-recorded seismicity (Fig. 1), including the 1915, Mw 7.0, Avezzano; 1997, Mw 6.0 Colfiorito; 2009, Mw

6.3, L’Aquila; and 2016, Mw 6.0 and 6.5, Amatrice-Norcia earthquakes. Although some of these mainshocks possibly nucleated within the crystalline basement (i.e., at ~8–10 km depths), it is well documented that many foreshocks and aftershocks as well as some mainshocks nucleated in and propagated through the overlying sedimentary sequence (Valoroso et al., 2013).

In the central Apennines, fault–fluid interaction has been documented at different crustal levels during seismic sequences. Miller et al. (2004) and Di Luccio et al. (2010) suggested that nearlithostatic fluid pressures at hypocentral depths triggered both mainshocks and aftershocks of the Colfiorito and L’Aquila earthquakes, respectively. Moreover, pore fluid diffusion has been invoked to explain the spatio-temporal migration of seismicity and the activation of different fault segments during the L’Aquila seismic sequence (Malagnini et al., 2012). Fluid–fault interaction has been recorded also at shallow crustal levels within groundwater aquifers. For instance, Favara et al. (2001), Italiano et al. (2001), Falcone et al. (2012), and Petitta et al. (2018) recorded an increase in fluid discharge and modifications of the groundwater chemistry soon after the Colfiorito, L’Aquila, and Amatrice-Norcia mainshocks. Moreover, Chioldini et al. (2011) constrained the seismic-related upward migration of mantle-derived deep-seated fluids towards shallow groundwater aquifers after the L’Aquila seismic sequence. Recently, Barberio et al. (2017) recorded changes in springs geochemistry a few months before and during the Amatrice-Norcia sequence, ascribing these changes to pre- and co-seismic shallow input of deep metal- and CO₂-rich fluids. This evidence indicates that fault activity in the central Apennines is associated with fluid circulation in the crust, with effects on the seismic cycle.

2.2. The Val Roveto Fault

The Val Roveto Fault (VRF; Fig. 1) belongs to the extensional tectonic setting of the central Apennines and bounds the NE margin of the Val (valley) Roveto. It is a ~60 km long potentiallyseismogenic fault (e.g., Roberts and Michetti, 2004), characterized by a polyphase tectonic history (Montone and Salvini, 1992; Ciotoli et al., 1993; Roberts and Michetti, 2004; Fabbri, 2016; Figs. 1 and 2). At surface, the VRF juxtaposes Messinian sandstones and marls (syn-orogenic deposits) located in the fault hangingwall (Castorina et al., 1994) and Mesozoic carbonates (pre-orogenic deposits) located in the fault footwall, showing, in places, up to 2,000 m of displacement (Fig. 2; Roberts and Michetti, 2004). In particular, the VRF can be divided into two segments (i.e., the northwestern and southeastern segments), which are characterized by different kinematics.

(1) The northwestern segment (Fig. 1) is characterized by highly-deformed shear zones showing strike-slip left-lateral movements (Montone and Salvini, 1992) and by NE-dipping (80°) fault planes showing left-lateral transpressional movements (Ciotoli et al., 1993; Fabbri, 2016). These shear zones and fault planes developed during the compressional tectonic phase that generated the Apennines fold-thrust belt and have been interpreted as transpressional pop-up structures (Ciotoli et al., 1993). At present, this part of the VRF is probably inactive (Roberts and Michetti, 2004).

(2) The southeastern segment is characterized by SW-dipping (40–80°) fault planes showing dip-slip extensional and left-lateral transtensional movements. Such fault planes were generated during the post-orogenic extensional tectonics and are kinematically consistent with the present seismogenic extensional tectonic setting of the central Apennines. In particular, Roberts and Michetti (2004) consider this segment of the VRF as presently seismogenic. In this paper, we focus our analyses on three exposures, namely Capistrello, Civitella Roveto, and San Giovanni, located along the southeastern segment of the VRF (Fig. 2).

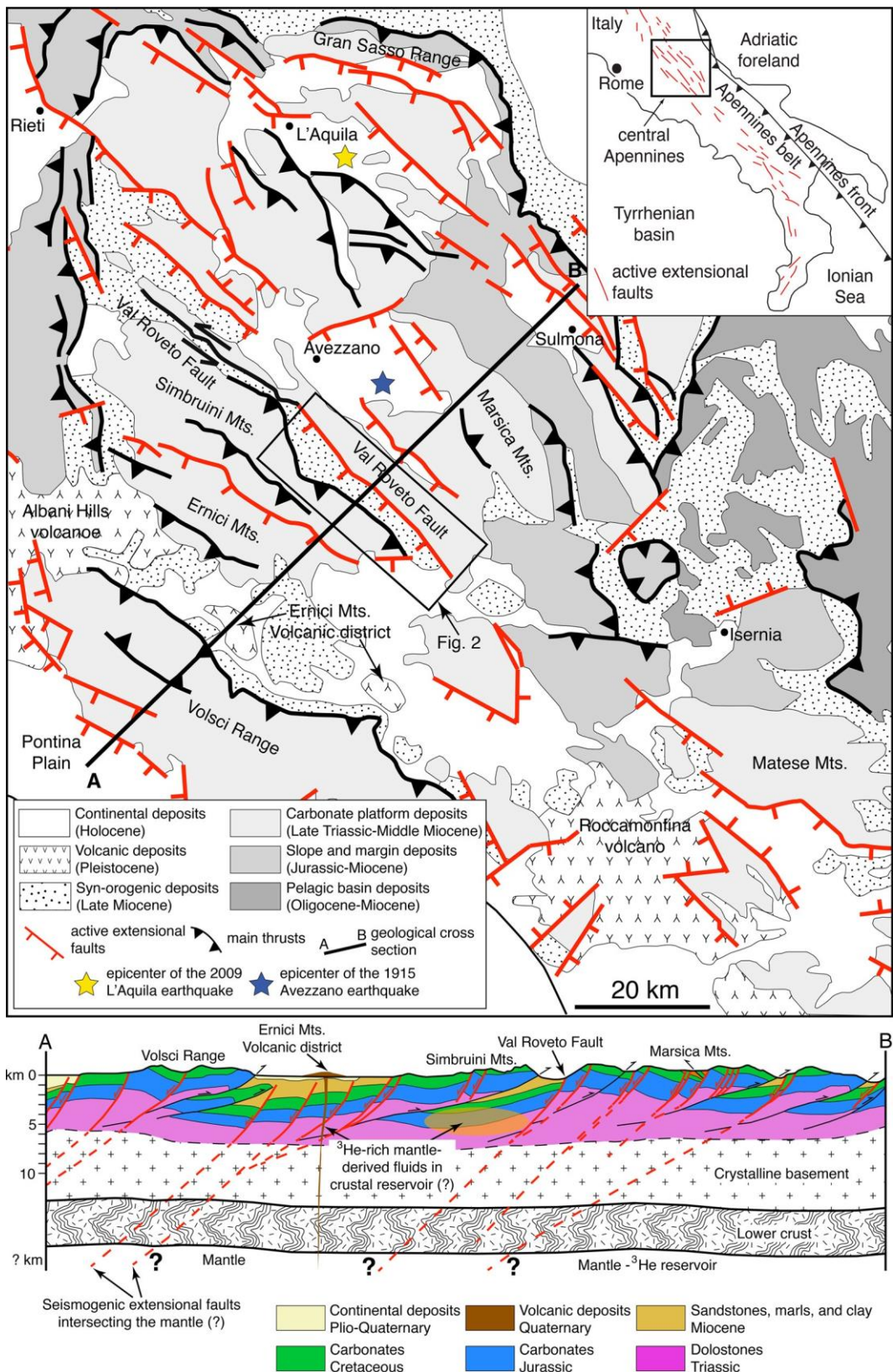


Fig. 1. Simplified geological map of the central Apennines (Italy), showing main thrusts, main active extensional faults, and location of the study area, i.e., Val Roveto Fault (VRF). Inset shows a schematic tectonic setting of the central-southern Italy with the Apennines thrust front and active extensional faults. Below, simplified geological cross-section through the central Apennines, showing main thrusts, main active extensional faults, and location of the hypocenter zones of major extensional fault-related earthquakes. (For interpretation of the colors in the figure(s), the reader is referred to the web version of this article.)

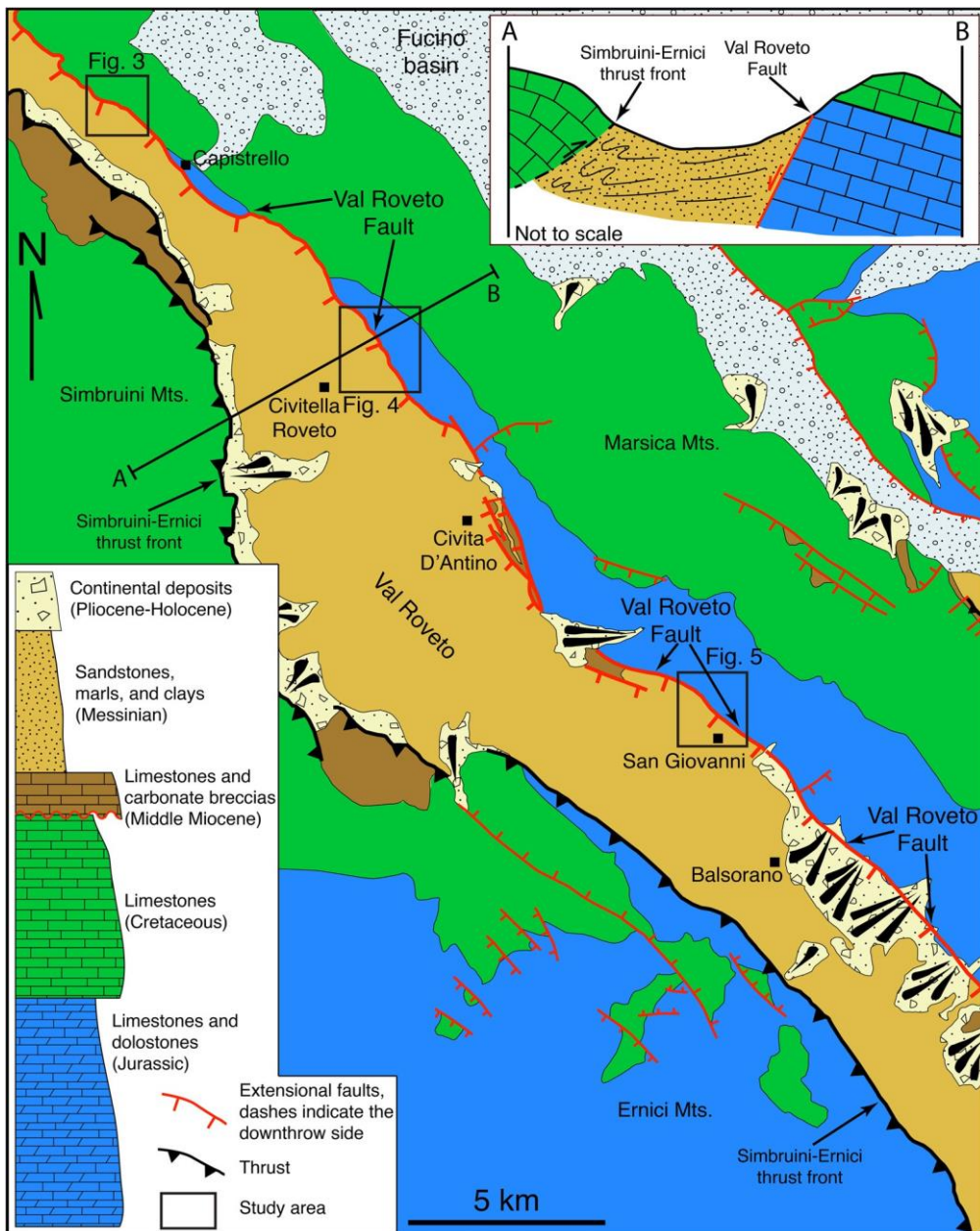


Fig. 2. Simplified geological map of the Val Roveto area showing the Simbruini-Ernici thrust front, the Val Roveto Fault, and the simplified stratigraphy of the study area. Inset shows a schematic cross-section through the Simbruini-Ernici thrust front and the Val Roveto Fault. The map shows the location of the three study exposures (Capistrello, Fig. 3; Civitella Roveto, Fig. 4; and San Giovanni, Fig. 5).

3. Methods

To reach our aim, we combined different methods including: 1:5,000 scale geological mapping and structural analyses; optical and cathodoluminescence (CL) microscopy; whole rock geochemistry; ^{13}C -, ^{18}O -, and $^{87}\text{Sr}/^{86}\text{Sr}$ -isotopes; carbonate clumped isotopes; H_2O , CO_2 , N_2 , and minor gaseous species (He, Ne, and Ar concentrations and isotope ratios) in fluid inclusions; and U-series dating of fault-related mineralizations. The analytical methods are fully described in the supplementary material.

4. Terminology and definitions

In this study, we adopt the terminology proposed by Hancock and Barka (1987) and Stewart and Hancock (1990) for extensional fault-related structures. Along the VRF, we recognized two main types of calcite-filled fractures: comb veins (C-veins) and slip-parallel veins (SP-veins) (Fig. 3a). C- and SP-veins are theoretically oriented perpendicular to the fault surface whereas their intersection with the fault surface generates lineations that are perpendicular (C-veins) and parallel (SP-veins) with respect to the downdip slip direction (Fig. 3a). In natural structures, these angular relationships are often less straightforward than in theory (Hancock and Barka, 1987; Stewart and Hancock, 1990; Doblas et al., 1997; Collettini et al., 2014). The angular relationships between C- and SP-veins, the principal surface and the slip vector along the VRF will be described in detail below.

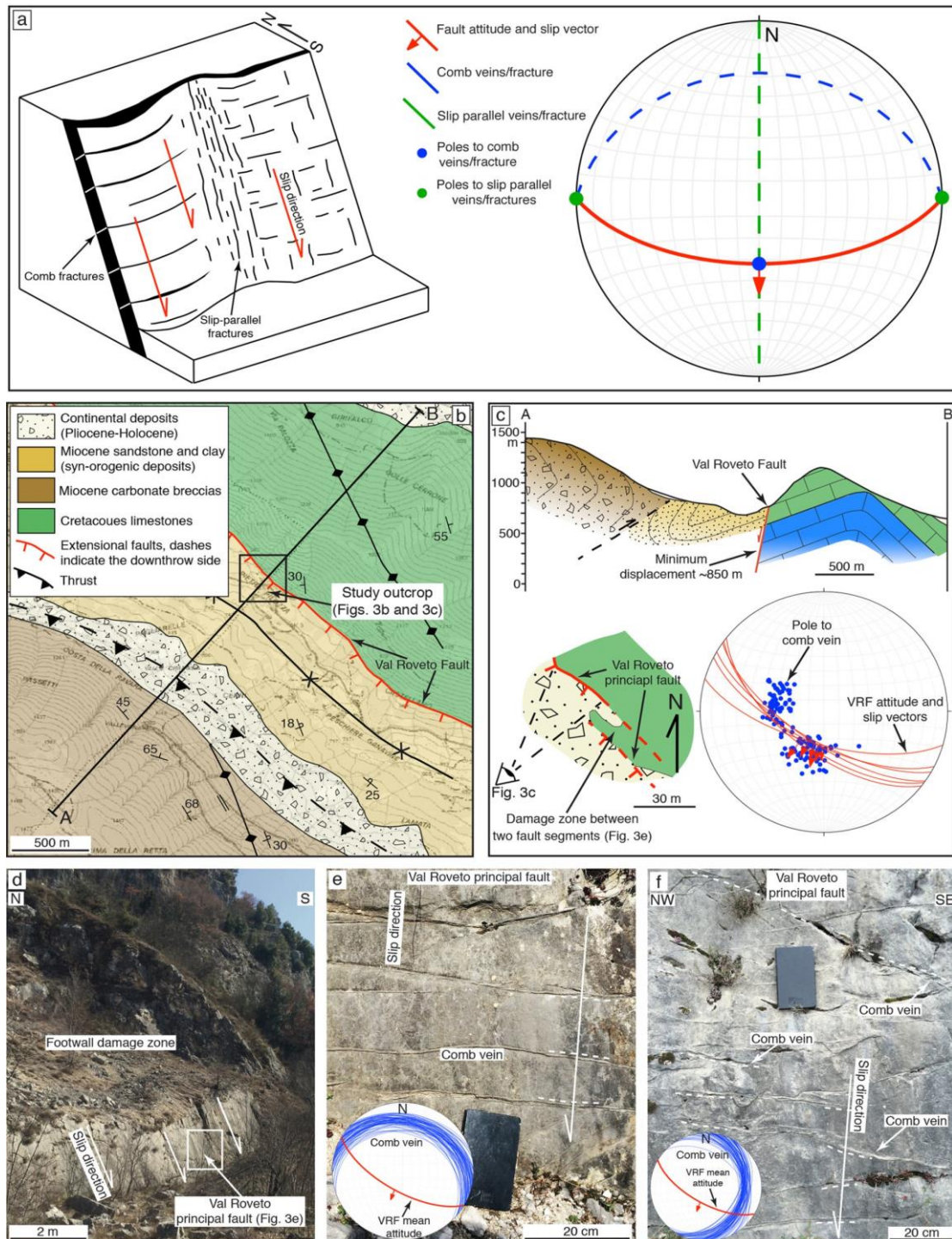


Fig. 3. (a) Conceptual cartoon showing comb and slip-parallel fractures/veins developed along an active extensional fault due to co-seismic stress release (modified after Stewart and Hancock, 1990). Schmidt net (lower hemisphere) for attitude and slip vector of an extensional fault (dip slip movement) with the typical attitude of related comband slip parallel-veins (see also Hancock and Barka, 1987). Comb- and slip parallel-veins are perpendicular and parallel to fault slip direction, respectively. (b) Simplified geological map of the Capistrello area created both from original field data and from previous mapping by Fabbri (2016). (c) Geological cross-section through the Val Roveto Fault in the Capistrello exposure area. Cross-section trace is shown in (a). Detailed structural map of the Capistrello exposure showing the two parallel en-echelon segments of the Val Roveto Fault and the damage zone in between them. Schmidt net (lower hemisphere) for attitude and slip vectors of the Val Roveto principal fault and poles to comb veins. (d) Panoramic view of the northeastward fault segment. Schmidt net (lower hemisphere) of comb vein attitude. (e, f) Comb veins along the Val Roveto Fault principal surface. Schmidt net (lower hemisphere) of comb vein attitude. Note the intersection lineations between comb veins and the fault plane. Lineations lie at high angles to fault slip direction.

5. Field observations

5.1. Fault exposures

In the three studied exposures, the VRF principal surface crops out along SW-dipping (40–80°) carbonate-hosted fault scarps, which are characterized by stratigraphic separations and slickenlines/grooves indicating dip-slip and left-lateral transtensional movements (Figs. 3b–d, 4a–c and 5a–c). In particular, in the Capistrello and Civitella Roveto exposures, the VRF consists of two parallel SW-dipping (65–70°) fault segments organized with a dextral en-echelon pattern (Figs. 3c and 4b). A damage zone occurs in Mesozoic limestones between the two parallel fault segments (Figs. 3c and 4b). In the Civitella Roveto exposure, the damage zone is also bounded by a NE-dipping (70–90°) antithetic fault showing dip-slip extensional and left-lateral transtensional slickenlines (Figs. 4b,c).

5.2. Fault-related mineralizations

The principal surface of the VRF and the related damage zone are cut by calcite-filled C- and SP-veins (see section 4) showing mutual crosscutting relations (Figs. 3, 4, 5, S1 and S2). The intersection of C- and SP-veins with the principal fault surface generates lineations characterized by rather variable angles with respect to the fault slip direction. In particular, for angles ranging between 45° and 90° we classify veins as C-veins (Figs. 3c,e,f, 4e–g, 5f, S1a–c and S1f) whereas for angles ranging between 0° and 45° we classify veins as SP-veins (Figs. 4g, 5f and S1f,h). We will comment on and explain these angles in the discussion section. In places, veins are characterized by undulated and anastomosing geometries and/or by abrupt changes in orientation, thus hindering an accurate classification into C- or SP-veins. Regardless of their angular relationship with the slip direction, C- and SP-veins show three main orientations: (1) NNW-to-ENE-dipping (5°–35°; Figs. 3e, 4b, and 5b), (2) ENE-to-SE-dipping (25°–65°; Figs. 3f and 5f), and (3) NW-to-SE-dipping (80°–90°; Fig. 4g).

C-veins are well exposed and visible in all three exposures (Figs. 3, 4, 5 and S1), whereas SP-veins are mostly developed in the San Giovanni exposure (Figs. 5f and S1h) and almost absent and very thin in the Capistrello and Civitella Roveto exposures (Figs. 4g and S1f). C- and SP-veins are up to 2-cm-thick and up to 2 m-long extensional features. In places, they can be also characterized by small (less than 2–3 cm) shear offsets, hence dissecting the principal fault surface in a drawer-like fashion (Figs. 4d,e,g, 5c,f–h, S1b,e, and S1f–h). Shear C- and SP-veins are often coated by calcite slickenfibers (Figs. 4d, 4g, 5g,h, and S1g,h). Offsets of the principal fault surface together with calcite slickenfibers indicate dip-slip reverse, dip-slip normal, left-lateral transpressional, or right-lateral transpressional movements along sheared veins (Figs. 4e and S1e). In particular, in the San Giovanni exposure, the principal fault surface is dissected by NE-dipping (40°–90°) SP-veins showing the largest shear offsets (from a few decimeters up to almost 1 meter) with respect to the other two exposures (Figs. 5c and 5h). In the San Giovanni exposure, the vein shear motion is either dip-slip reverse or oblique transpressional (Fig. 5h).

In places, C- and SP-veins are characterized by anastomosing and mutually-abutting geometries generating a pervasive high-density network. In particular, thin veins merge together to form non-systematic clusters, which fully affect and overprint the fault surface generating textures similar to those of fault-fracture meshes (*sensu* Sibson, 2000; Figs. 5d,e and S1d,h).

6. Vein microstructures

At the microscale, C- and SP-veins are characterized by crack and seal textures (e.g., Ramsay, 1980) showing multiple generations of calcite crystals with blocky to elongated-blocky morphologies (Figs. 6a–c, S3a and 9). Close to the vein walls, multiple and less than 100 µm-thick layers of calcite crystals are separated by sub-parallel wall-rock layers (Figs. 7a and S3a; e.g., Holland and Urai, 2010), constituting nucleation sites for the new calcite crystal growth. The sub-parallel wall-rock layers occur also within the veins far away from the walls (Fig. 6b). Calcite crystals symmetrically grew either from the vein walls or from the wall-rock layers towards the center of the vein, evolving from elongated-blocky crystals, with well-developed growth competition textures, to blocky crystals in the vein center (Figs. 6a–c and S3a). In places, crystals are truncated by sharp surfaces, which are in turn the nucleation site for new crystal generations (Figs. 6e and 9). In addition, thin veins (<50 µm-thick) with anastomosing geometries occur as dense clusters, which fully overprint the cataclastic texture, generating a mesh-like texture similar to that observed at the mesoscale within the San Giovanni exposure (compare Figs. 6d and S3c,d with Figs. 5d,e).

Observations in CL light (Figs. 6f, S3b and S3e,f) show the occurrence of different phases of calcite precipitation characterized by different CL colors. CL zonation within crystals highlights the symmetrical crystal growth from the walls to the center of the veins.

Slickenfibers consist of multiple layers of calcite crystals showing blocky to fibrous morphologies separated by sub-parallel shear surfaces (Figs. 6g,h and 9). Fibrous crystals show long axes oriented roughly parallel with respect to shear surfaces (Fig. 9). Within crystal layers, multiple subparallel inclusion bands with micrometer-thick separations occur at high angles (~60°–70°) to the shear surfaces (Figs. 6g,h). Slickenfibers grew by micrometer-thick slip increments on the shear surface, associated with dilation in microscopic dilational jogs, and calcite precipitation in the newly created dilational sites (Figs. 6h and 9; e.g., Fagereng and Byrnes, 2015). In places, slickenfibers develop above extensional C- and SP-veins, promoting vein shearing and the generation of sheared C- and SP-veins (Fig. 6i).

7. Geochemistry

7.1. Carbon, oxygen and clumped isotopes

Results from the stable isotope analyses are shown in Fig. 7a and listed in Table S1. Results are reported in the conventional δ-notation with respect to the Vienna Pee Dee Belemnite (VPDB) for δ¹³C and Vienna Standard Mean Ocean Water (VSMOW) for δ¹⁸O. The host rock δ¹³C and δ¹⁸O values range between +1‰ and +3‰, and between +28‰ and +30‰, respectively. Such values are typical of Jurassic-Cretaceous marine carbonates in central Apennines, Italy (e.g., Agosta and Kirchner, 2003; Smeraglia et al., 2016). C-vein δ¹³C and δ¹⁸O values range between +2‰ and -9‰, and between +25‰ and +35‰, respectively. The δ¹⁸O values are close to those of the host rock in the San Giovanni exposure but markedly enriched compared to the host rock at Capistrello. At Civitella Roveto, both δ¹⁸O and δ¹³C values are rather variable. SP-vein δ¹³C and δ¹⁸O values range between 0‰ and -17‰, and between +24‰ and +32‰, respectively, and are characterized by δ¹³C values more negative than those of C-veins. At Civitella Roveto, SP-veins are characterized by a narrow range of δ¹⁸O values between +24‰ and +25‰ and by a large range of δ¹³C values between -3‰ and -8‰. Calcite slickenfibers are generally characterized by a narrow range of δ¹³C values and by a large range of δ¹⁸O values. However, there are also four samples with negative δ¹³C values ranging between -8‰ and -16‰.

We measured also δ¹³C and δ¹⁸O of different calcite generations (up to four generations) within three C-veins (sample 127,

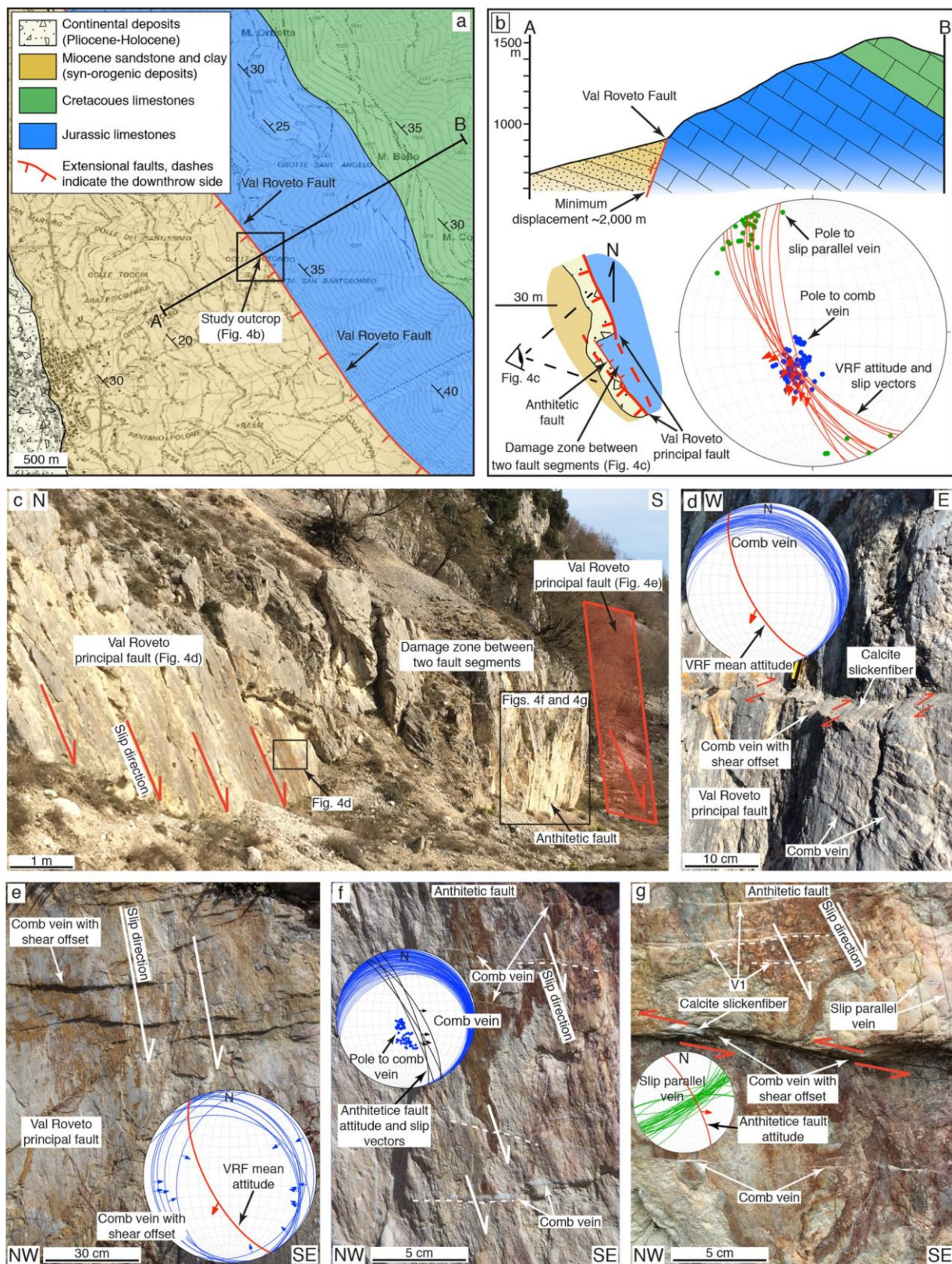


Fig. 4. Civitella Roveto exposure. **(a)** Simplified geological map of the Civitella Roveto area. **(b)** Geological cross-section through the Val Roveto Fault within the Civitella Roveto exposure. Cross-section trace in (a). Detailed structural map of the Civitella Roveto exposure showing the two parallel en-echelon segments of the Val Roveto Fault and the damage zone in between. Schmidt net (lower hemisphere) for attitude and slip vectors for the Val Roveto Fault principal surface and poles to comb and slip-parallel veins. **(c)** Panoramic view of the segmented Val Roveto Fault and the damage zone between the two parallel fault segments. **(d, e)** Comb veins across the Val Roveto Fault principal surface. Schmidt net (lower hemisphere) of comb vein attitude. **(e)** Comb veins with drawer-like geometry across the Val Roveto Fault principal surface. Note the intersection lineations between comb veins and the fault plane. Lineations lie at high angles to fault slip direction. Sheared comb veins coated by calcite slickenfibers show dip-slip reverse, right-lateral, or left-lateral transpressional movements. **(f, g)** Comb and slip-parallel veins along an antithetic fault of the VRF within the main damage zone. Schmidt net (lower hemisphere) for comb and slip-parallel vein attitude. Note the intersection lineations between comb and slip-parallel veins and the fault plane, at high angles and parallel to the slip direction, respectively.

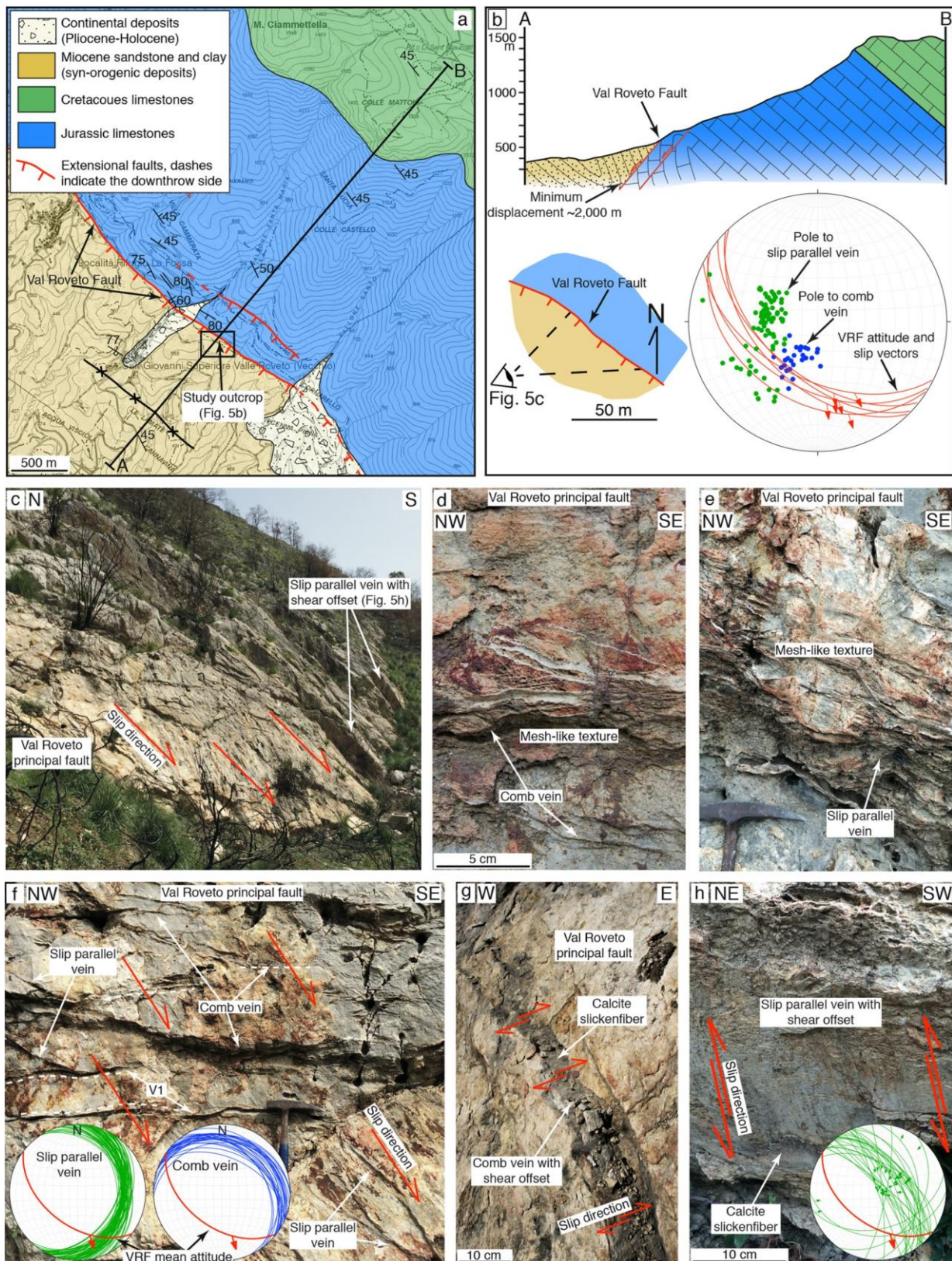


Fig. 5. San Giovanni Vecchio exposure. **(a)** Simplified geological map of the San Giovanni area. **(b)** Cross-section through the Val Roveto Fault within the San Giovanni exposure. Geological cross-section trace in (a). Structural map of the San Giovanni exposure. Schmidt net (lower hemisphere) for attitude and slip vectors of the Val Roveto Fault and poles to comb and slip-parallel veins. **(c)** Panoramic view of the Val Roveto Fault showing slip-parallel veins dissecting the principal fault plane. **(d, e)** Mesh-like pattern including both comb and slip-parallel veins. Note the thin veins that merge together from large vein clusters, which completely pervade and overprint the principal fault. **(f)** Comb and slip-parallel veins along the Val Roveto Fault. Schmidt net (lower hemisphere) for comb and slip-parallel vein attitude. Note the intersection lineations between comb and slip-parallel veins and the fault plane. These lineations are oblique, for comb veins, and parallel, for slip-parallel veins, to the slip direction. **(g)** The Val Roveto Fault principal surface dissected by comb veins with shear offset, coated with calcite slickenfibers. **(h)** Detail of a slip-parallel vein with shear offset coated with calcite slickenfibers indicating dip-slip reverse movement. Schmidt net (lower hemisphere) for attitude and slip vectors of slip-parallel vein with shear offsets.

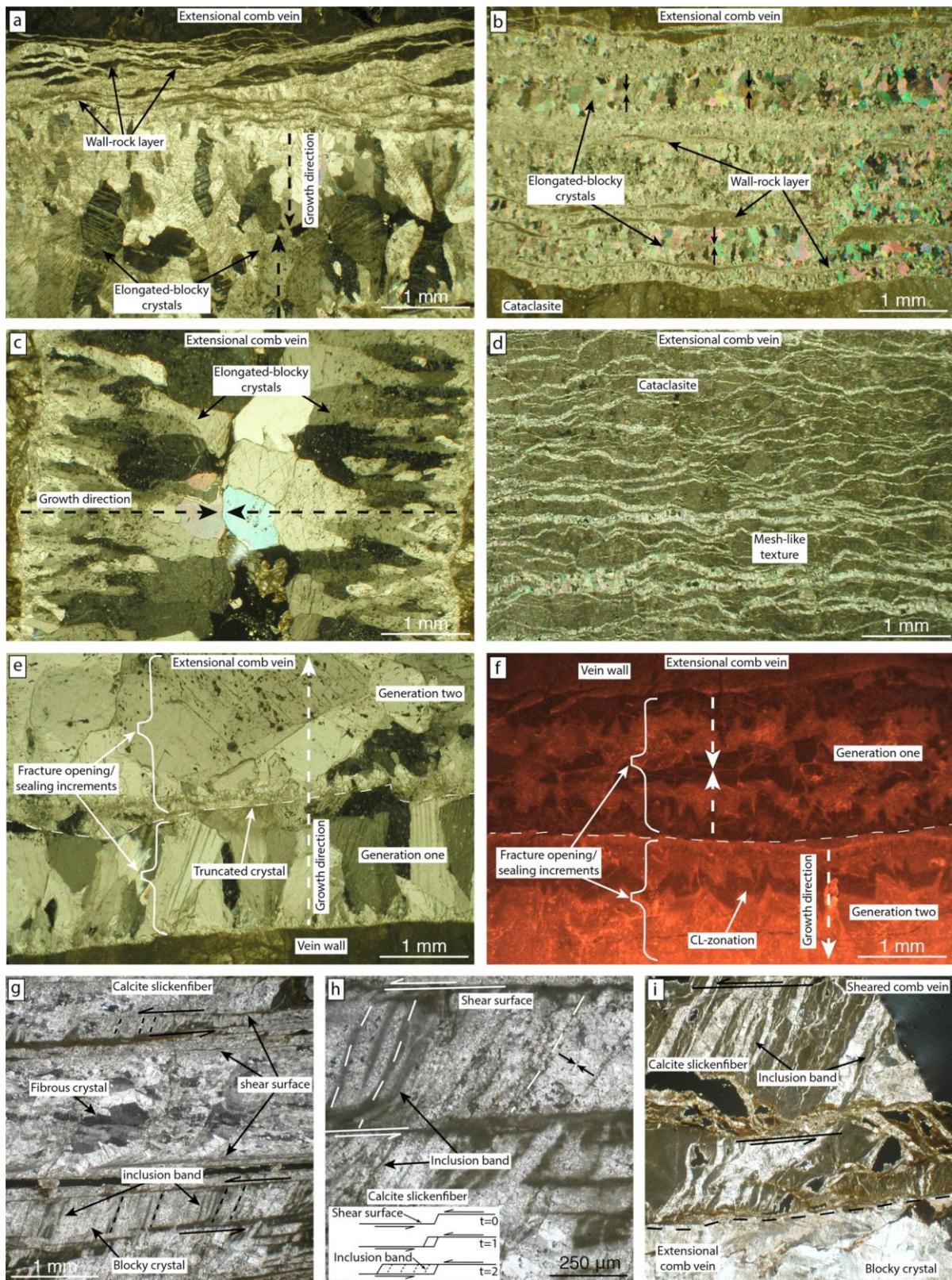


Fig. 6. Microstructures from fault-related mineralizations taken from thin sections under cross-polarized light and cathodoluminescence light (CL). (a, b) Crack and seal textures of comb and slip-parallel veins showing multiple wall-rock layers parallel to vein walls. Note the different sizes of incremental opening. Calcite crystals texture varies from blocky to elongated-blocky, showing syntaxis growth. (c) Single crack and seal event showing well developed elongated-blocky calcite crystals with syntaxis growth. (d) Mesh-like texture at the macroscale. Compare it with the mesh-like texture at the microscale (Fig. 5d and 5f). (e) Detail of sharply truncated crystals showing two generations of calcite cement. Each crystal generation indicates crack and seal event. (f) Microphotograph under CL showing two different events of calcite precipitation highlighted by different CL colors. These colors indicate slight changes in fluid chemistry within each precipitation event. Note CL-zonation indicating changes in fluid chemistry during crystal precipitation. (g, h) Slickenfiber textures showing multiple calcite crystal layers bounded by multiple shear surfaces. Note multiple inclusion bands at high angles ($\sim 60\text{--}70^\circ$) with respect to the shear surfaces. Inset in (h) shows the typical model for the development of slickenfibers by incremental dilation along two parallel shear surfaces (modified after Fagereng and Byrnes, 2015). (i) Sheared C-vein showing slickenfiber above extensional vein wall.

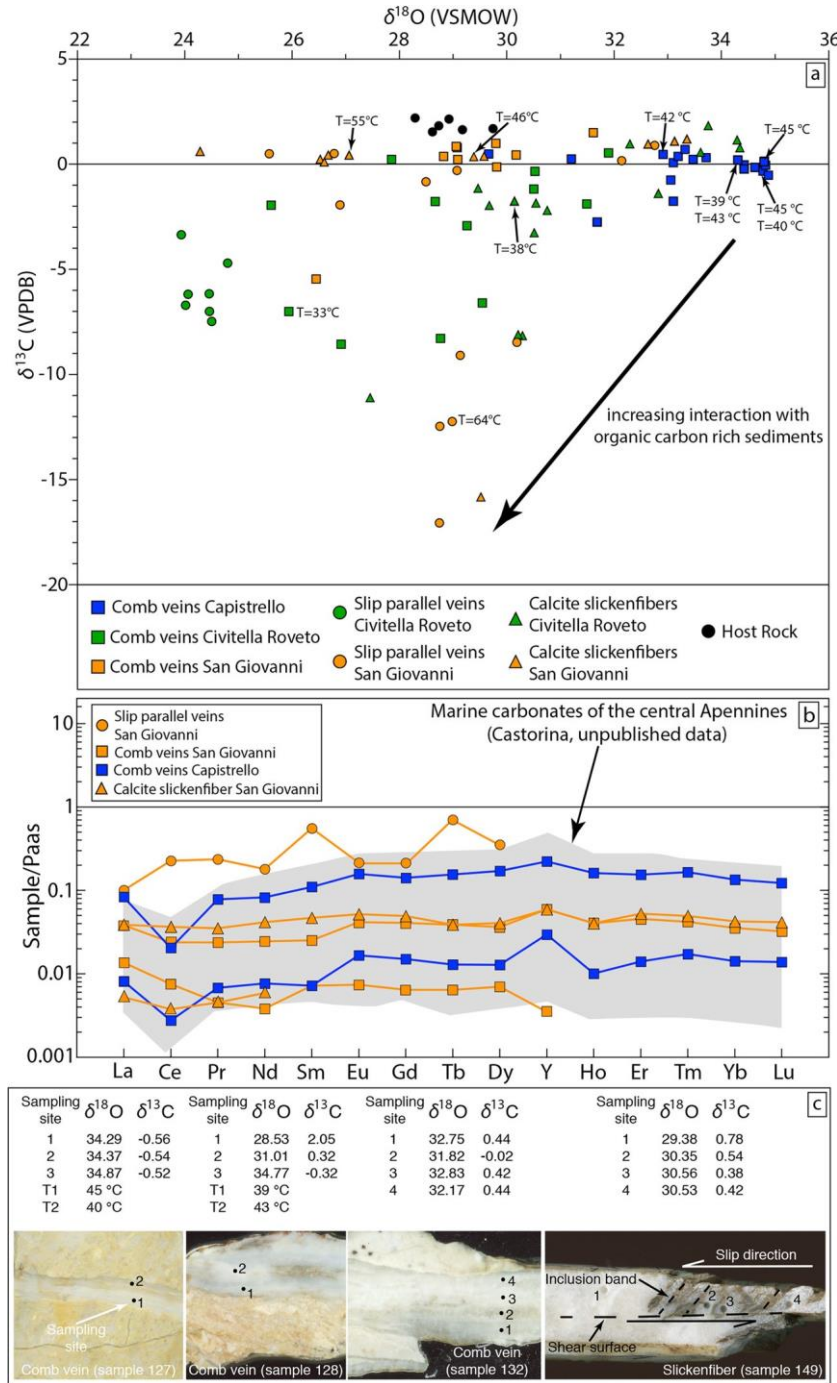


Fig. 7. (a) $\delta^{13}\text{C}$ (PDB) versus $\delta^{18}\text{O}$ (VSMOW) diagram for the analyzed samples from various mineralizations (veins and sickenfibers) and carbonate rocks in the three exposures and surrounding area. (b) PAAS-normalized REE-patterns of comb and slip-parallel veins and sickenfibers from the VRF. Note the low REE concentration with respect to marine carbonates and the preserved Ce and Y anomalies inherited from marine carbonates.

128, and 132) and one calcite sickenfiber (sample 149; Fig. 7c). Results show that multiple calcite generations can be characterized by similar (samples 127, 132 and 149) or also different (sample 128) $\delta^{13}\text{C}$ and $\delta^{18}\text{O}$ values (Fig. 7c). Clumped isotopes are reported in the carbon dioxide equilibration scale (CDES) with uncertainty in temperature reported at the 95% confidence level.

Clumped-isotope data from 11 veins and sickenfibers sampled 0.681 (Table S2). Using a revised version of the Kele et al. (2015) in the three exposures yields ΔA_{47} values between 0.567 and 0.681‰ (Table S2). Using a revised version of the Kele et al. (2015) calibration (see Methods), these values correspond to temperatures between $\sim 32 \pm 11$ °C and $\sim 64 \pm 3$ °C (Table S2 and S5). In particular, C-veins precipitated at $\sim 32 \pm 11$ °C (sample 18), $\sim 47 \pm 9$ °C (sample 129), and $\sim 42 \pm 5$ °C (sample 132); SP-veins precipitated at $\sim 64 \pm 3$ °C (sample 61); and calcite sickenfibers precipitated at $\sim 38 \pm 4$ °C (sample 25), $\sim 55 \pm 7$ °C (sample 58), and $\sim 46 \pm 11$ °C (sample 149). We performed also clumped-isotope measurements on two different generations of calcite precipitates within two C-veins (samples 127 and 128) from the Capistrello exposure (i.e., two measurements for each vein). Calcite precipitated at temperatures of $\sim 45 \pm 13$ °C and $\sim 40 \pm 8$ °C in sample 127, and at temperatures of $\sim 39 \pm 10$ °C and $\sim 43 \pm 6$ °C in sample 128 (Fig. 7c).

Summarizing, we identify temperature clusters within the three exposures: samples from Capistrello, Civitella Roveto, and San Gio-

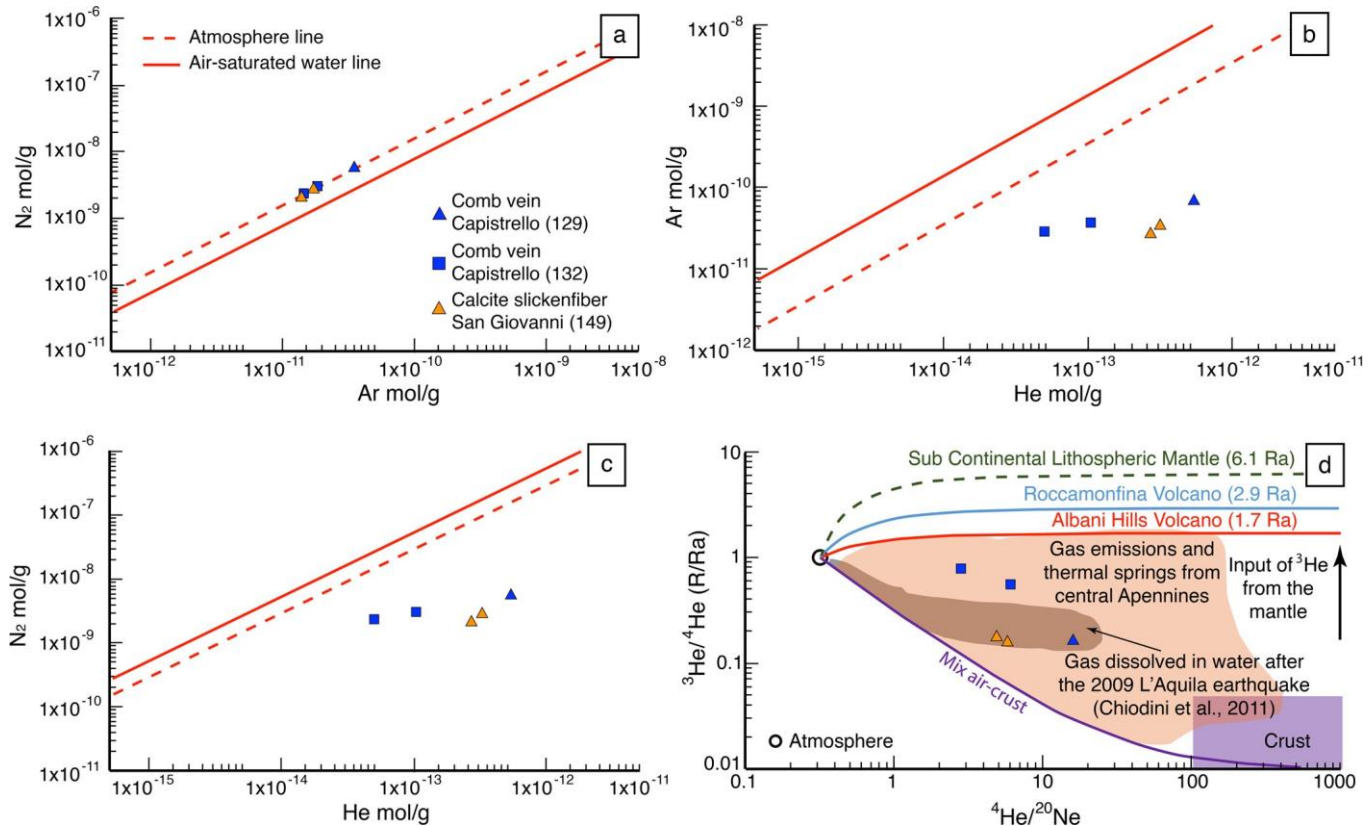


Fig. 8. Fluid inclusions data for the analyzed samples from fault-related mineralizations (comb veins and calcite slickenfibers). Both the atmosphere line and the air-saturated water line (at standard pressure and temperature conditions) are reported. (a) Ar (mol/g) versus N₂ (mol/g) diagram. Note that the measured values fall along the N₂/Ar Atmosphere line. (b) He (mol/g) versus Ar (mol/g) and (c) He (mol/g) versus N₂ (mol/g) diagrams. Note that the measured values fall both below the Atmosphere line and below the Air-saturated water line, indicating an excess of He in fluids circulating during calcite precipitation. (d) ⁴He/²⁰Ne ratio versus ³He/⁴He (R/Ra) ratio diagram. Note that the ³He/⁴He ratios of sample 129 (comb vein) and of calcite slickenfiber fall within the range of gases and thermal springs from the central Apennines, whereas sample 132 (comb vein) shows the highest mantle contribution. The Roccamontina and Albani Hills volcanic signature (i.e., volcanoes located in central Apennines near the VRF) are from Martelli et al. (2004).

vanni show precipitation temperatures between $\sim 39 \pm 10$ °C and $\sim 45 \pm 13$ °C (samples 127, 128, 129, and 132), between $\sim 32 \pm 11$ °C and $\sim 38 \pm 4$ °C (samples 18 and 25), and between $\sim 46 \pm 11$ °C and $\sim 64 \pm 3$ °C (samples 58, 61, and 149), respectively.

7.2. ⁸⁷Sr/⁸⁶Sr-isotopes, Sr concentration, and REY-elements pattern

C-veins (samples 104, 129, and 132), SP-veins (sample 61), and calcite slickenfibers (samples 114 and 149) show ⁸⁷Sr/⁸⁶Sr-isotope values ranging between 0.7078 and 0.7087 (Table S5, analytic error for temperatures in Table S2). These values are slightly lower than those of Late Miocene seawater (0.7089; McArthur et al., 2001) and of Messinian syn-orogenic deposits (0.7089; Castorina et al., 1994), and slightly higher than those of the Jurassic to Cretaceous carbonates (0.7068–0.7078; McArthur et al., 2001).

Sr concentrations within the analyzed mineralizations range between 214 and 519 ppm, with only one sample showing a lower value around 108 ppm (Table S5). These Sr concentrations are similar to those of the Jurassic-Cretaceous carbonates (e.g., Veizer, 1983) and markedly higher than those of calcite cement precipitated from meteoric-derived fluids (26 to 87 ppm; Agosta and Kirschner, 2003) in fault rocks of other nearby extensional faults in the central Apennines.

REE abundances in veins and slickenfibers show large variations, ranging from 0.25 to 17.7 mg/kg (Table S3). The PAAS-normalized REY-patterns show that REE concentrations are in the range of those from the Mesozoic carbonates of the central Apennines (Fig. 7b; Castorina, unpublished data). All samples show LREE depletion (Nd_{PAAS}/Yb_{PAAS} = 0.64–0.98), negative Ce anomaly, and a marked positive Y anomaly (mass ratio of Y to Ho), typically observed in marine carbonates (Fig. 7b).

7.3. U-series dating

We dated two C-veins (samples 129 and 132) from the Capistrello exposure, one SP-vein (sample 61) from the San Giovanni exposure, and one slickenfiber on a C-vein (sample 149) from the San Giovanni exposure. The age of C-veins are 146 ± 2 ky (sample 129) and 121 ± 1 ky (sample 132), respectively, the age of the SP-vein is 150 ± 2 ky (sample 61), and the age of the C-vein slickenfiber is 317 ± 49 ky (sample 149) (Table S4 for complete data). We consider these ages reliable as microstructural observations show that these veins are not affected by calcite recrystallization, which would have obliterated the primary crystals.

7.4. Fluid inclusions composition

The concentrations of H₂O, CO₂, N₂, light noble gases (He, Ne, Ar), and ³He/⁴He, ⁴He/²⁰Ne, ⁴⁰Ar/³⁶Ar isotope ratios within fluid inclusions hosted in C-veins (samples 129 and 132) and calcite slickenfibers (sample 149) are reported in Table S6, whereas the N₂ vs. Ar and He vs. Ar

ratios are plotted in Fig. 8 and listed in Table S6. H₂O and CO₂ show concentrations ranging between 6.6×10^{-6} and 2.4×10^{-5} mol/g and between 2.9×10^{-8} and 3.5×10^{-8} mol/g, respectively (Fig. S4a). The N₂/Ar ratios range between 80.0 and 82.7 (Fig. 8a). These values are consistent with the N₂/Ar ratio in the atmosphere (N₂/Ar =

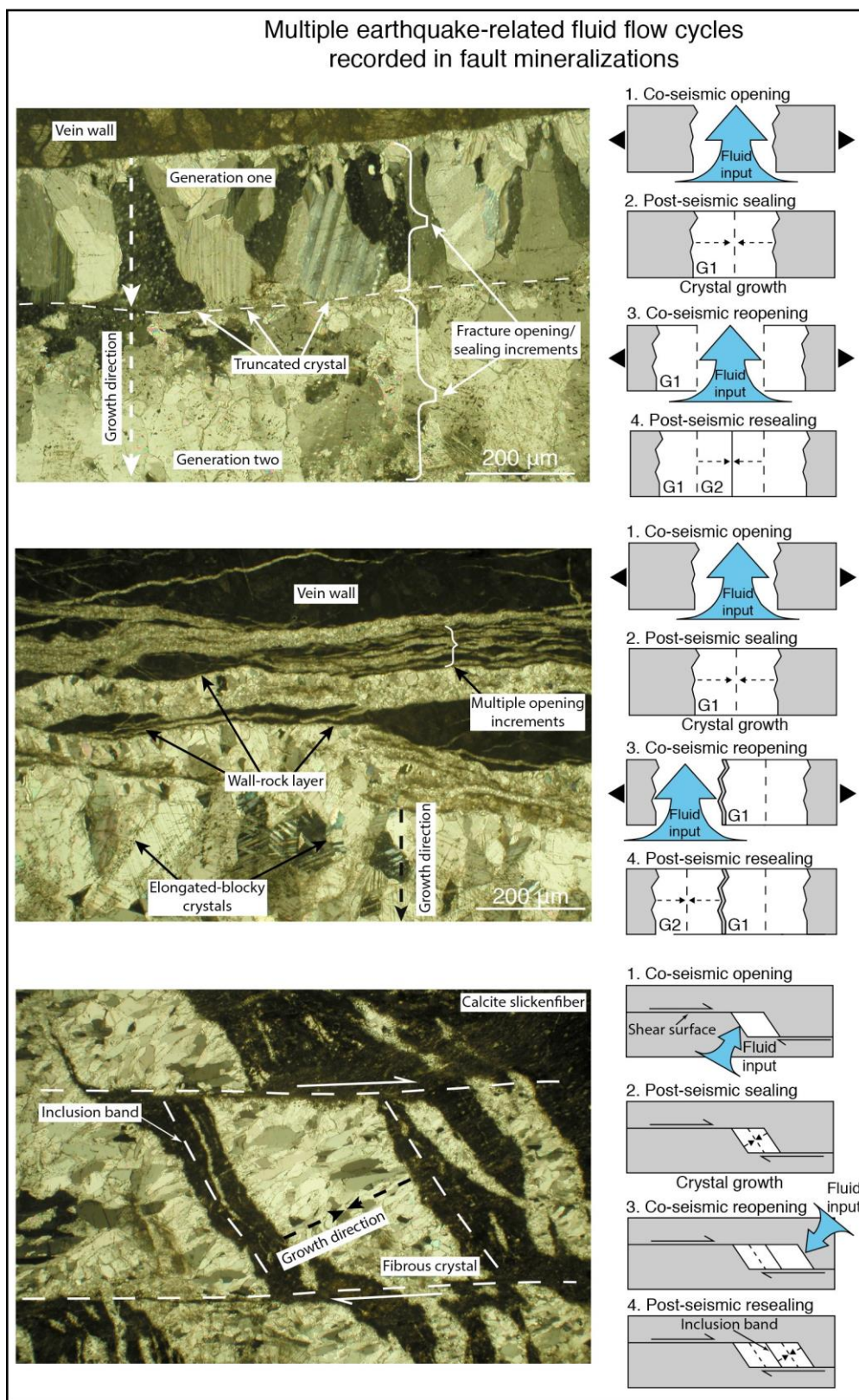


Fig. 9. Schematic illustration of multiple earthquake-related fluid flow cycles preserved within fault-related mineralization microstructures (veins and slickenfibers). In particular, the illustration shows temporal relationships between multiple episodes of fracture opening and sealing. G1 and G2 denote the earliest cements precipitated following consecutive fracture opening, and therefore record the approximate timing of co-seismic fracture opening (modified after Williams et al., 2017).

84.1) and are markedly higher than the N₂/Ar ratio in air-saturated water at standard temperature and pressure (N₂/Ar = 38). The ⁴⁰Ar/³⁶Ar ratios (ranging between 300.2 and 314.1) are also close to the ⁴⁰Ar/³⁶Ar ratio in the atmosphere (⁴⁰Ar/³⁶Ar = 295.5; Table S6). On the contrary, He/Ar and He/N₂ ratios are more than one order of magnitude higher than the theoretical values both in the atmosphere and in the air-saturated water (Figs. 8b,c). Also the ⁴He/²⁰Ne ratios (ranging between 2.8 and 15.8) are 9 to 50 times higher than the typical ⁴He/²⁰Ne ratio in the atmosphere (⁴He/²⁰Ne = 0.318; Fig. 8d and Table S6).

The ³He/⁴He ratios, corrected for the air contamination using the measured ⁴He/²⁰Ne ratio, range between 0.16 and 0.78 Ra (Fig. 8d), showing a lack of correlation with He concentrations (Fig. S4b). Using the measured U and Th concentrations (Table S4) and the estimated ages of the analyzed veins, we exclude any significant contribution of radiogenic ⁴He accumulation due to U and Th decay (Fig. S4b). In particular, the ⁴He produced in 146 ky (sample 129) and in 121 ky (sample 132) is 3.3×10^{-14} and 2.9×10^{-14} , respectively. These values are one order of magnitude lower than the He values measured in both C-veins (He = $1\text{--}10 \times 10^{-13}$ mol/g).

8. Discussion

8.1. Vein development

We base the interpretation of VRF-related mineralizations on geometrical and temporal evidence and on analogy with similar structures from the literature (Hancock and Barka, 1987; Stewart and Hancock, 1990).

Concerning the time of veining, U-series ages show that calcite precipitated in Late Pleistocene time along the VRF. Therefore, fault-related mineralizations precipitated during the extensional phase that affected the central Apennines (i.e., since Early Pliocene; Cavinato and De Celles, 1999) and generated the VRF. The U-series dating can be used to hypothesize the depth of calcite precipitation along the VRF. Considering a slip rate of ~ 1.1 mm/a (i.e., estimated by Roberts and Michetti, 2004), we calculated that samples 129 (C-vein), 132 (C-vein), 61 (SP-vein), and 149 (slickenfiber along C-vein) precipitated at depths of ~ 160 m, ~ 133 m, ~ 165 m, and ~ 349 m, respectively, below the present-day outcrop altitude (between ~ 800 and ~ 1000 m a.s.l.). In the following, we use this temporal/depth evidence together with geometrical evidence and analogies with previous studies to interpret and constrain the genesis of the veins.

We interpret fault-related mineralizations along the VRF as calcite-filled comb fractures and slip-parallel fractures due to their attitude and angular relationships with fault surface and slip directions. In particular, the intersection of C-veins and SP-veins with respect to the fault surface generates lineations that are at high angles (between $45^\circ\text{--}90^\circ$) and at low angles (between $0^\circ\text{--}45^\circ$) with respect to the slip direction (Fig. 10a). This finding recalls observations reported from other shallow active extensional faults in the Aegean region, southern Spain, Turkey, and northern Apennines (e.g., Hancock and Barka, 1987; Stewart and Hancock, 1990; Doblas et al., 1997; Collettini et al., 2014). In places, C- and SP-fractures can be characterized by up to a few centimeters of either normal or reverse shear offsets (e.g., Hancock and Barka, 1987; Stewart and Hancock, 1990; Doblas et al., 1997; Collettini et al., 2014), as observed along the VRF (compare figure 6d from Hancock and Barka, 1987 with Figs. 4e, and 5f from this study). C- and SP-fractures are commonly interpreted as structures developed at depths <500 m (consistently with the VRF case), linked to stick-slip displacement episodes and/or multiple displacement increments during seismic slip along extensional fault planes (Hancock and Barka, 1987). These fractures initiate as extensional features (i.e., tension cracks) reflecting the co-seismic down-dip stretching of the footwall block due to local stress release and/or reorientation (Hancock and Barka, 1987; Stewart and Hancock, 1990) or to tear effects related to the gravitational collapse of the hangingwall block along the fault plane and consequent pull of the footwall block (Doglioni et al., 2015). Therefore, C- and SP-veins develop perpendicular or parallel to slip direction of the hangingwall block (i.e., highlighted by slickenlines and grooves along the fault surface; Hancock and Barka, 1987; Stewart and Hancock, 1990). However, we observed a slight discrepancy with the theoretical angles between C- and SP-veins and related fault surfaces and slip directions (Figs. 3a and 10a). We explain such a discrepancy suggesting that fault slip direction may have changed during time. In this scenario, kinematic indicators allow to constrain the last or best-preserved fault slip motion, whereas the C- and SP-veins may have developed during previous slip episodes.

Pre-existing extensional fractures/veins can be reactivated by further co-seismic stress release episodes as shear veins that offset the fault surface (Stewart and Hancock, 1990). Episodic displacements and/or multiple stick-slip episodes are consistent with the crack and seal textures observed within fault-related mineralizations along the VRF (Fig. 6). In particular, each crack and seal event implies crack opening, blocky to elongated-blocky crystals precipitation from an advective flow in a fluid-filled open crack (Hilgers et al., 2004), and consequential crack sealing (Fig. 9). In our studied case, new cracking events occurred only after the complete sealing of fractures, as shown by well-developed wall rock inclusion bands and sharp crystal truncations (Fig. 9; e.g., Williams et al., 2017).

The studied C-, SP-veins, and slickenfibers are characterized by variable sizes of the incremental crack and seal growth (up to 5 mm for a single crack event, Fig. 6a–c) within the same vein. Fagereng and Byrnes (2015) proposed that these variable sizes are consistent with different slip increment magnitudes or different fault slip styles, including slow, fast, and intermediate slip rates. We speculate that, in the case of the central Apennines, the different sizes of incremental crack and seal growth in C-, SP-veins, and slickenfibers may account for small-to-large slip events recorded along extensional faults at shallow depths ($\leq\sim 350$ m) by crack episodes of different magnitudes. This incremental growth may, in particular, be consistent with recent extensional seismic sequences that lasted for months-to-years with tens of thousands of earthquakes of various magnitudes (Colfiorito 1997, L'Aquila 2009, and Amatrice-Norcia 2016 sequences; e.g., Valoroso et al., 2013; Chiaraluce et al., 2017).

The attitude of C- and SP-veins further supports the genetic link with earthquakes. The Andersonian stress condition (i.e., shallow) implies, in extensional tectonic settings, a vertical maximum stress and horizontal minimum and intermediate stresses. Under this assumption, extensional fractures and veins should be subvertical and perpendicular to the minimum stress. Along the VRF, we documented C- and SP-veins that are oriented inconsistently with respect to the Andersonian stress field associated with extensional faults. The same applies to previously documented C- and SP-fractures/veins (Hancock and Barka, 1987; Stewart and Hancock, 1990). Therefore, as previously interpreted (Hancock and Barka, 1987), we suggest that C- and SP-veins were generated by local stress conditions and deformation mechanisms (stretching or tear effects) developed during seismic events along the VRF principal surface.

8.2. Fluid sources

Geochemical data are consistent with calcite precipitation from warm fluids (paleofluid temperatures between ~ 32 and ~ 64 °C) consisting of meteoric-derived fluids modified by reactions with crustal rocks and with a mantle contribution (e.g.,

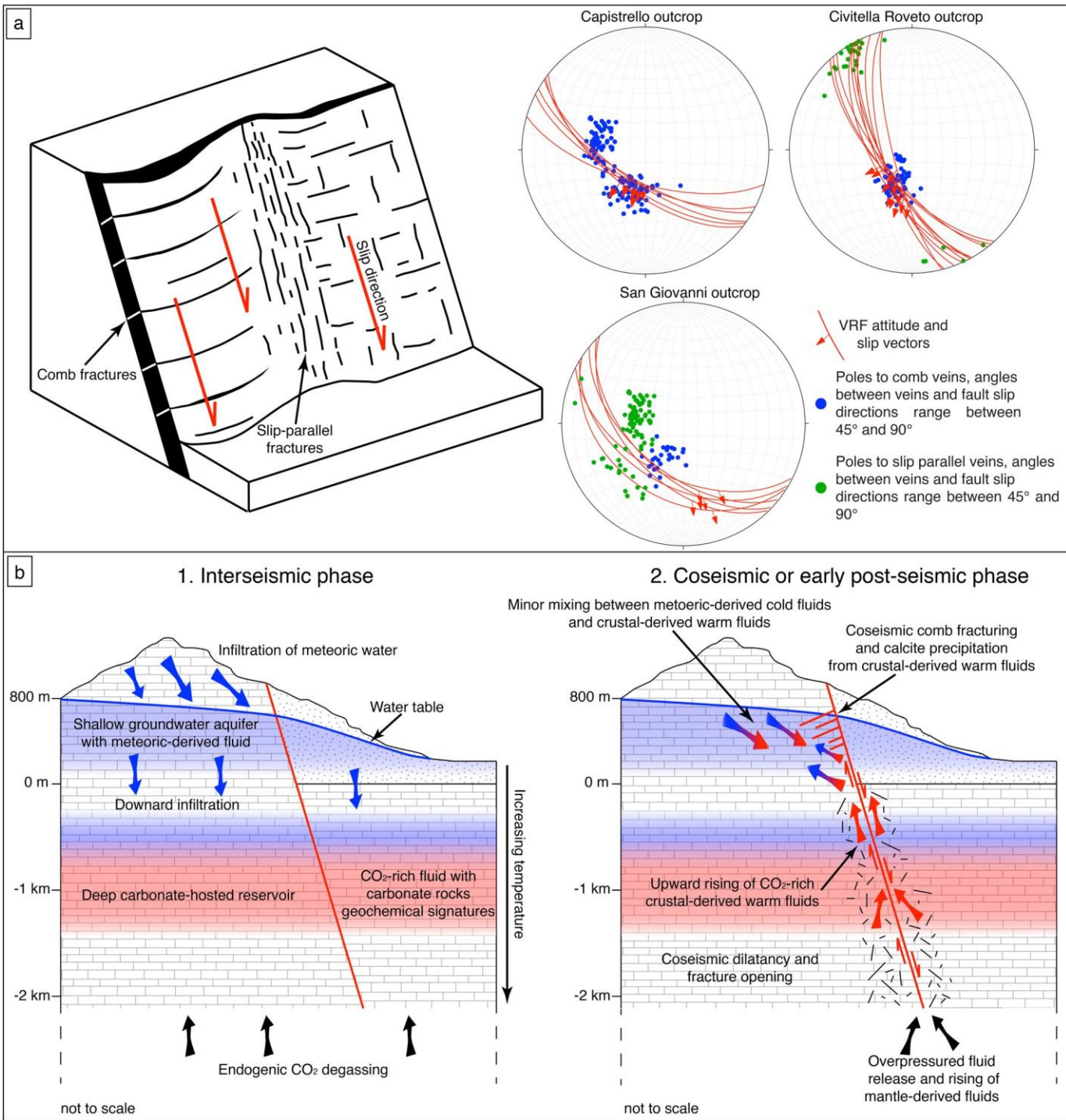


Fig. 10. (a) Conceptual cartoon showing comb and slip-parallel fractures/veins commonly developed along active extensional faults due to co-seismic stress release (modified after Stewart and Hancock, 1990). Schmidt net (lower hemisphere) for attitude and slip vectors of the Val Roveto Fault principal surface and poles to comb and slip-parallel veins in the three study exposures. (b) Cartoon showing the conceptual model for seismic-related fluid circulation implying: (1) the downward infiltration of meteoric water and/or shallow groundwater into carbonate-hosted reservoirs at depth and consequent fluid heating and fluid–rock interactions; and (2) earthquake-related squeezing and fast ascent of deep-seated fluids along fault. As a consequence, calcite precipitation occurs at shallow (≤ 350 m) depths within co-seismic or early post-seismic comb and slip-parallel fractures.

Uysal et al., 2011; Ünal-İmer et al., 2016), with minor and local mixing with meteoric waters at shallow levels. We base this interpretation on the following evidence:

(1) The calculated $\delta^{18}\text{O}_{\text{paleofluid}}$ composition, which was in equi-librium with the calcite at the time of mineral growth, ranges between $-0.9\text{\textperthousand}$ and $+10.2\text{\textperthousand}$ according to the O’Neil et al. (1969) equation and the calculated clumped isotope temperatures (Table S5). These values indicate ^{18}O enrichment due to oxygen exchange between the fluids and the crustal carbonate rocks.

(2) The $^{87}\text{Sr}/^{86}\text{Sr}$ -isotope values of all samples are lower than those of Messinian syn-orogenic deposits and higher than those of Mesozoic carbonate deposits of the study area (Table S5). Therefore, the $^{87}\text{Sr}/^{86}\text{Sr}$ -isotope values may result from isotope exchanges between the paleofluid and the crustal carbonate

rocks of the study area. This is consistent with the Ce and Y anomalies (Fig. 7b) and high Sr concentrations (Table S5), indicating a strong fluid–rock interaction (crustal level) and a marine carbonate imprinting preserved by the paleofluid. A strong fluid–rock interaction is also consistent with the REY concentrations of the studied samples, which are in the range of those from marine carbonates of the central Apennines, indicating a long residing time within the crustal carbonate-hosted reservoirs.

(3) Data from fluid inclusions suggest an excess of He in fluids circulating during calcite precipitation, indicating a source of He other than the atmosphere (Figs. 8b,c). In particular, the $^3\text{He}/^4\text{He}$ ratios fall within the range of gases and thermal springs from the central Apennines (Fig. 8d; e.g., Minissale, 2004; Caracausi and Paternoster, 2015). Samples 129 (C-vein) and 149 (calcite slickenfibers) indicate a crustal-derived fluid enriched in ^4He with small ^3He mantle contribution of ~6% and ~10%, respectively (assuming an average $^3\text{He}/^4\text{He}$ of 0.17 Ra; Fig. 8d). In addition, sample 132 (C-vein) shows the highest ^3He mantle contribution of ~23% and ~39%, assuming a local mantle $^3\text{He}/^4\text{He}$ ratio of 1.7 and 2.9 (i.e., measured for the nearby Roccamonfina and Colli Albani volcanoes; Martelli et al., 2004), respectively. This evidence suggests the input and mixing of mantle-derived fluids at the time of C-veins precipitation. Overall, these values are similar to those of crustal-derived fluids (with limited mantle contribution) enriched in ^4He recorded in some springs of the central Apennines (Italiano et al., 2001; Chiodini et al., 2011).

Based on the above-discussed evidence, we infer that fault-related mineralizations sampled along the VRF, although precipitated at shallow (≤ 350 m) depths where cold meteoric water and/or shallow groundwater dominate, preserve geochemical signatures indicating strong fluid–rock interaction and crustal imprinting at warm temperatures with a mantle contribution. We exclude a pure meteoric origin of the paleofluid for the following reasons:

(1) the calculated $\delta^{18}\text{O}_{\text{paleofluid}}$ compositions (Table S5) are significantly enriched in ^{18}O with respect to the modern meteoric waters (~7–9‰ VSMOW, average composition of rainfall in central Apennines; Minissale, 2004) and to spring water and/or shallow groundwater (~8–11‰ VSMOW in the central Apennines; Minissale, 2004) from the shallow carbonate aquifers of the central Apennines; paleofluid temperatures, ranging between 32 and 64 °C (Table S5), are higher than water temperatures both for most spring waters (i.e., recorded at surface) and for carbonate aquifers (i.e., recorded at depth in tunnels) along the axial region of the central Apennines, ranging between 6 and 24 °C (e.g., Chiodini et al., 2000; Minissale, 2004; Falcone et al., 2008);

(2) the Sr concentrations (Table S5) are markedly higher than those of (a) fault-related mineralizations precipitated from meteoric-derived fluids within other nearby extensional faults in the central Apennines (Agosta and Kirschner, 2003), (b) groundwater from shallow carbonate aquifers in central Apennines (Minissale, 2004), and (c) Sr-poor meteoric waters. Only one sample (sample 102) shows Sr concentration of 104 ppm (i.e., the lowest of the whole dataset, Table S5), probably indicating local dilution with Sr-poor fluids such as shallow groundwater and/or meteoric waters;

(3) The $\delta^{13}\text{C}$ values are consistent with those of the carbonate host-rocks, implying that the carbon is derived from dissolution of the host-rocks. However, several fault-related mineralizations show a markedly more negative $\delta^{13}\text{C}$ values. We suggest that light carbon derives from the oxidation of organic matter from the sedimentary succession beneath the VRF. In particular, organic matter is present in Messinian syn-orogenic deposits and in Mesozoic carbonate rocks, such as Upper Triassic bituminous dolostones (e.g., Cosentino et al., 2010).

We cannot completely exclude minor and local mixing with meteoric waters or shallow groundwater with negative $\delta^{13}\text{C}$ values, which range between -2‰ and -15‰ in the central Apennines (e.g., Minissale, 2004). These latter fluids may have partially contributed to light carbon enrichment in the mineralizing paleofluid. In addition, mixing with meteoric-derived waters is also consistent with both the N_2/Ar and $^{40}\text{Ar}/^{36}\text{Ar}$ ratios, which are close to those calculated for the atmosphere (Fig. 8a and Table S6), thus indicating an atmospheric component dissolved in the mineralizing paleofluid.

8.3. Seismic-related fluid circulation

We propose a general model of seismic-related fluid circulation that is consistent with the above-discussed structural and geochemical evidence.

Interseismic phase (Fig. 10a). Meteoric waters infiltrated through a high-permeability fracture network of the brittle crust and accumulated within carbonate-hosted reservoirs at shallow crustal depths. Due to fluid–rock interaction, the fluid became enriched in ^{18}O , acquired a geochemical signature approaching that typical of the carbonate host-rock, and was heated according to the geothermal gradient. In addition, due to continuous endogenous CO_2 degassing (e.g., Chiodini et al., 2000), the fluid became CO_2 -enriched and hence $\text{Ca}(\text{HCO}_3)_2$ -rich due to the interaction with the carbonate host-rock.

Co-seismic to early post-seismic phase (Fig. 10b). During earthquakes, co-seismic dilatancy (i.e., fracture opening; e.g., Sibson, 2000) promoted the upward squeezing of the fluid along the fault plane (e.g., Doglioni et al., 2014; Petitta et al., 2018) and fluid mixing with meteoric-derived waters at shallow depth, favored by the co-seismic disruption of impermeable barriers trapping overpressured fluids at depth (e.g., Sibson, 2000). This is consistent with the observed increase in surface fluid discharge in springs and wells (e.g., Falcone et al., 2012; Barberio et al., 2017; Petitta et al., 2018) and with geophysical data suggesting release of high-pressure CO_2 -rich fluids during earthquakes or early postseismic phases in the central Apennines (Miller et al., 2004). Sudden fluid depressurization and ascent, coupled with seismic shaking, can foster rapid CO_2 degassing causing carbonate oversaturation and consequent calcite precipitation into shallow (≤ 350 m) co-seismic C- and SP-fractures.

The proposed evolution is consistent with the suction pump model of Sibson (2000), describing earthquake-fluid interactions within extensional faults. In particular, the suction pump model implies co-seismic dilatancy, the upward drainage of fluids, and transient fluid depressurization into newly created extensional fractures. Extensional fault-fracture meshes can occur at shallow depths (i.e., depths < 3 km) and close to the surface, as observed along the VRF, under hydrostatic fluid pressure (e.g., Sibson, 1993, 2000).

A number of evidence suggests dynamic fluid flow cycles and multiple fluid pulse episodes even at the scale of the single vein (Fig. 9; e.g., Williams et al., 2017). Multiple veining episodes are documented by the observed crack-and-seal textures (Figs. 6 and S3), varying CL colors (Figs. 6f, S3b and S3f), CL-zonations (Figs. 6f, S3b and S3f), variable $\delta^{13}\text{C}$ and $\delta^{18}\text{O}$, and different precipitation temperatures within individual veins (Fig. 7c). Such multistage fluid circulation and calcite precipitation are consistent with that documented in other seismically-active extensional settings (e.g., Uysal et al., 2011; Ünal-Imer et al., 2016).

The different paleofluid temperatures recorded within the three exposures, Capistrello between ~39 °C and ~45 °C, Civitella Roveto between ~32 °C and ~38 °C, and San Giovanni between ~46 °C and ~64 °C, suggest that, below the three outcrops, paleofluids may have been located at slightly different crustal depths characterized by different temperatures due to different local geothermal gradients. Alternatively, the temperature differences could be also related to different cooling rates during fluid ascent and/or mixing with warmer or colder fluids.

Several veins from San Giovanni formed at warm temperatures from fluids with a relatively low ^{18}O -enrichment whereas other veins from Civitella Roveto and Capistrello were formed at lower temperatures from fluids more enriched in ^{18}O (Fig. 7a). The lack of direct correlation between temperature and ^{18}O -enrichment, which would be expected for a simple model of deep vs. shallow origin of the fluids, can be explained by the fact that the $\delta^{18}\text{O}$ of the fluid is controlled by the extent of water-rock interaction at depth, which is a function of both temperature and water/rock ratio. Fluids that circulated in low permeability rocks (low water/rock ratio) at shallow depths may have experienced more extensive enrichment in ^{18}O than fluids that circulated to greater depths through more fractured/permeable rocks (high water/rock ratio). The scatter in $\delta^{18}\text{O}$ and $\delta^{13}\text{C}$ values suggests different degrees of mixing between fluids that have experienced variable degrees of water-rock interaction and circulation through different host rocks.

Summarizing, we suggest that multiple co-seismic dilatancy and fracture opening along the VRF created high-permeability pathways and structural connection through the upper crust, allowing interaction and mixing between different fluids from different depths and sources, also with mantle signature. Such high-permeability pathway is still active along the VRF, as suggested by soil gas measurements indicating an ongoing degassing of deep endogenic gases (Ciotoli et

al., 1993). However, we cannot discriminate between the two following scenarios: (1) the VRF constitutes a physical connection with deep crustal reservoirs enriched in mantle-derived fluids (i.e., derived by degassing magmatic intrusions or by lithospheric discontinuity); (2) the VRF constitutes a lithospheric discontinuity down to the mantle (Fig. 1).

9. Conclusions

Calcite-filled comb and slip-parallel veins occur along the fault plane of the active extensional Val Roveto Fault. In accordance with previous works (Hancock and Barka, 1987; Stewart and Hancock, 1990), we interpret both comb and slip-parallel veins as co-seismic or early post-seismic features developed as a result of multiple displacement episodes linked with seismic slip along the fault. Veins precipitated in the Late Pleistocene at shallow ($\lesssim 350$ m) depths from warm fluids with temperatures between ~ 32 and ~ 64 °C consisting of meteoric-derived waters modified by reactions with crustal rocks and with a mantle contribution.

Structural and geochemical data are consistent with a general model of earthquake-related fluid circulation implying: (1) the downward infiltration of meteoric and/or shallow groundwater-derived fluids into carbonate-hosted reservoirs at crustal depths and consequent fluid heating and fluid–rock interactions with the carbonate host-rock, and (2) earthquake-related squeezing and rapid ascent of deep-seated crustal and mantle fluids along the fault zone, with consequent mixing with meteoric waters and calcite precipitation at shallow ($\lesssim 350$ m) depths in co-seismic comb and slip-parallel fractures. We propose that cyclic events of co-seismic fracturing, deep-seated fluid ascent, and vein precipitation affected the VRF.

Comb and slip-parallel veins/fractures were discovered and qualitatively described several years ago (e.g., Hancock and Barka, 1987; Stewart and Hancock, 1990). Since then, their importance and significance have been perhaps underestimated. The results from our study coupled with the evidence that these structures are rather common, particularly along seismogenic extensional faults (e.g., Stewart and Hancock, 1990; Doblas et al., 1997; Collettini et al., 2014), require further studies to test the co-seismic origin of these fractures/veins in different settings. If our model is confirmed at other locations, these structures may become fundamental to unravel the seismic-related fluid circulation along extensional faults within the brittle upper crust. As most carbonate veins can be radiometrically dated, carbonate comb and slip-parallel veins may become a unique and irreplaceable tool to unravel the seismic history of hazardous active faults.

Acknowledgements

This work has been funded by: PRIN2010/11 (Project 20107ESMX9) and Progetti di Ateneo Sapienza 2014 to E. Carminati; PRIN 2015 (Project 2015EC9PJ5_001) to C. Doglioni; Progetti di Ateneo Sapienza 2016 to L. Aldega and 2017 to E. Carminati; and Progetto di Avvio alla Ricerca 2016 (Sapienza) to L. Smeraglia. S. Bernasconi acknowledges support from the Swiss National Science Foundation, grant No. 200021_166282. We thank D. Mannetta and TS Lab & Geoservices for exceptional thin sections, I. Baneschi and M. Mola for help during sample preparation and isotope analyses, G.P. Cavinato for introducing us to the Val Roveto Fault outcrops, A. Cipriani, C. Collettini, S. Fabbri, M. Fondriest, C. Giorgetti, M. Mercuri, and E. Valerio for constructive discussions and help during fieldwork and sampling. We also thank M. Misseri and M. Tantillo for analyzing the chemistry of CO₂, H₂O, N₂, and isotope composition of light noble gases and M. Jaggi for clumped isotope analyses. We thank the editor J.P. Avouac, K. Ujiie and an anonymous reviewer for their comments, which improved and clarified the paper.

Appendix A. Supplementary material

Supplementary material related to this article can be found online at <https://doi.org/10.1016/j.epsl.2018.06.013>.

References

- Agosta, F., Kirschner, D.L., 2003. Fluid conduits in carbonate-hosted seismogenic normal faults of central Italy. *J. Geophys. Res.* 108, 2221. <https://doi.org/10.1029/2002JB002013>.
- Balsamo, F., Clemenzi, L., Storti, F., Mozafari, M., Solum, J., Swennen, R., Taberner, C., Tueckmantel, C., 2016. Anatomy and paleofluid evolution of laterally restricted extensional fault zones in the Jabal Qusaybah anticline, Salakht arch, Oman. *Geol. Soc. Am. Bull.* 128, 957–972. <https://doi.org/10.1130/B31317.1>.
- Barberio, M.D., Barbieri, M., Billi, A., Doglioni, C., Petitta, M., 2017. Hydrogeochemical changes before and during the 2016 Amatrice-Norcia seismic sequence (central Italy). *Sci. Rep.* 7, 11735. <https://doi.org/10.1038/s41598-017-11990-8>.
- Boullier, A.M., Fujimoto, K., Ohtani, T., Roman-Ross, G., Lewin, E., Ito, H., Pezard, P., Ildefonse, B., 2004. Textural evidence for recent co-seismic circulation of fluids in the Nohima fault zone, Awaji island, Japan. *Tectonophysics* 378, 165–181. <https://doi.org/10.1016/j.tecto.2003.09.006>.
- Caracausi, A., Paternoster, M., 2015. Radiogenic helium degassing and rock fracturing: a case study of the southern Apennines active tectonic region. *J. Geophys. Res.* 120, 2200–2211. <https://doi.org/10.1002/2014JB011462>.
- Carminati, E., Lustriño, M., Doglioni, C., 2012. Geodynamic evolution of the central and western Mediterranean: tectonics vs. igneous petrology constraints. *Tectonophysics* 579, 173–192. <https://doi.org/10.1016/j.tecto.2012.01.026>.
- Castorina, F., Cipollari, P., Cosentino, D., Di Biaso, E., Naso, G., Tallini, M., 1994. Testimonianza dell'evento a Gessi nei depositi dell'avvafossa della Val Roveto (Appenino centrale): considerazioni sull'estensione spazio-temporale dell'avvafossa messiniana. *Mem. Soc. Geol. Ital.* 51, 35–47.
- Cavinato, G.P., De Celles, P.G., 1999. Extensional basins in tectonically bimodal central Apennines fold-thrust belt, Italy: response to corner flow above a subducting slab in retrograde motion. *Geology* 27, 955–958. [https://doi.org/10.1130/0091-7613\(1999\)027<0955:EBITTB>2.3.CO;2](https://doi.org/10.1130/0091-7613(1999)027<0955:EBITTB>2.3.CO;2).
- Chiaraluce, L., Di Stefano, R., Tinti, E., Scognamiglio, L., Michele, M., Casarotti, E., Cattaneo, M., De Gori, P., Chiarabba, C., Monachesi, G., Lombardi, A., Valoroso, L., Marzorati, S., 2017. The 2016 central Italy seismic sequence: a first look at the mainshocks, aftershocks, and source models. *Seismol. Res. Lett.* 88, 757–771. <https://doi.org/10.1785/0220160221>.
- Chioldini, G., Frondini, F., Cardellini, C., Parello, F., Peruzzi, L., 2000. Rate of diffuse carbon dioxide Earth degassing estimated from carbon balance of regional aquifers: the case of central Apennine, Italy. *J. Geophys. Res.* 105, 8423–8443. <https://doi.org/10.1029/1999JB900355>.
- Chioldini, G., Caliro, S., Cardellini, C., Frondini, F., Ingugliato, S., Matteucci, F., 2011. Geochemical evidence for and characterization of CO₂-rich gas sources in the epicentral area of the Abruzzo 2009 earthquakes. *Earth Planet. Sci. Lett.* 304, 389–398. <https://doi.org/10.1016/j.epsl.2011.02.016>.
- Ciotoli, G., Etiope, G., Lombardi, S., Naso, G., Tallini, M., 1993. Geological and soil-gas investigations for tectonic prospecting: preliminary results over the Val Roveto Fault (Central Italy). *Geol. Rom.* 29, 483–493.
- Collettini, C., Carpenter, B.M., Viti, C., Cruciani, F., Mollo, S., Tesei, T., Trippett, F., Valoroso, L., Chiaraluce, L., 2014. Fault structure and slip localization in carbonate-bearing normal faults: an example from the Northern Apennines of Italy. *J. Struct. Geol.* 67, 154–166. <https://doi.org/10.1016/j.jsg.2014.07.017>.
- Cosentino, D., Cipollari, P., Marsili, P., Scrocca, D., 2010. Geology of the central Apennines; a regional review. *J. Virtual Explorer* 36. <https://doi.org/10.3809/jvirtex.2010.00223>.
- Di Luccio, F., Ventura, G., Di Giovambattista, R., Piscini, A., Cinti, F.R., 2010. Normal faults and thrusts reactivated by deep fluids: the 6 April 2009 Mw 6.3 L'Aquila earthquake, central Italy. *J. Geophys. Res.* 115. <https://doi.org/10.1029/2009JB007190>.
- Doblas, M., Mahecha, V., Hoyos, M., Lo'pez-ruiz, J., 1997. Slickenside and fault surface kinematic indicators on active normal faults of the Alpine Betic cordilleras, Granada, southern Spain. *J. Struct. Geol.* 19, 159–170. [https://doi.org/10.1016/S0191-8141\(96\)00086-7](https://doi.org/10.1016/S0191-8141(96)00086-7).
- Doglioni, C., Barba, S., Carminati, E., Riguzzi, F., 2014. Fault on-off versus co-seismic fluids reaction. *Geosci. Front.* 5, 767–780. <https://doi.org/10.1016/j.gsf.2013.08.004>.
- Doglioni, C., Carminati, E., Petricca, P., Riguzzi, F., 2015. Normal fault earthquakes or graviquakes. *Sci. Rep.* 5, 12110. <https://doi.org/10.1038/srep12110>.

- Evans, J.P., Forster, C.B., Goddard, J.V., 1997. Permeability of fault-related rocks, and implications for hydraulic structure of fault zones. *J. Struct. Geol.* 19, 1393–1404. [https://doi.org/10.1016/S0191-8141\(97\)00057-6](https://doi.org/10.1016/S0191-8141(97)00057-6).
- Fabbi, S., 2016. Geology of the Northern Simbruini Mts (Abruzzo-Italy). *J. Maps* 12, 441–452. <https://doi.org/10.1080/17445647.2016.1237899>.
- Fagereng, Å., Byrnes, G., 2015. A range of fault slip styles on progressively misoriented planes during flexural-slip folding, Cape Fold Belt, South Africa. *J. Struct. Geol.* 70, 156–169. <https://doi.org/10.1016/j.jsg.2014.12.001>.
- Falcone, R.A., Falgiani, A., Parisse, B., Petitta, M., Spizzico, M., Tallini, M., 2008. Chemical and isotopic ($\delta^{18}\text{O}$ ‰, $\delta^2\text{H}$ ‰, $\delta^{13}\text{C}$ ‰, ^{222}Rn) multi-tracing for ground-water conceptual model of carbonate aquifer (Gran Sasso INFN underground laboratory-central Italy). *J. Hydrol.* 357, 368–388. <https://doi.org/10.1016/j.jhydrol.2008.05.016>.
- Falcone, R.A., Carucci, V., Falgiani, A., Manetta, M., Parisse, B., Petitta, M., Rusi, S., Spizzico, M., Tallini, M., 2012. Changes on groundwater flow and hydrochemistry of the Gran Sasso carbonate aquifer after 2009 L'Aquila earthquake. *Ital. J. Geosci.* 131 (3), 459–474. <https://doi.org/10.3301/IIG.2011.34>.
- Favarra, R., Italiano, F., Martinelli, G., 2001. Earthquake-induced chemical changes in the thermal waters of the Umbria region during the 1997–1998 seismic swarm. *Terra Nova* 13, 227–233. <https://doi.org/10.1046/j.1365-3121.2001.00347.x>.
- Hancock, P.L., Barka, A.A., 1987. Kinematic indicators on active normal faults in western Turkey. *J. Struct. Geol.* 9, 573–584. [https://doi.org/10.1016/0191-8141\(87\)90142-8](https://doi.org/10.1016/0191-8141(87)90142-8).
- Hilgers, C., Dilg-Gruschnitski, K., Urai, J.L., 2004. Microstructural evolution of syntectonic veins formed by advective flow. *Geology* 32, 261–264. <https://doi.org/10.1130/G20024.1>.
- Holland, M., Urai, J.L., 2010. Evolution of anastomosing crack-seal vein networks in limestones: insight from an exhumed high-pressure cell, Jabal Shams, Oman Mountains. *J. Struct. Geol.* 32, 1279–1290. <https://doi.org/10.1016/j.jsg.2009.04.011>.
- Italiano, F., Martinelli, G., Nuccio, P.M., 2001. Anomalies of mantle-derived helium during the 1997–1998 seismic swarm of Umbria-Marche, Italy. *Geophys. Res. Lett.* 28, 839–842. <https://doi.org/10.1029/2000GL012059>.
- Kele, S., Breitenbach, S.F., Capezzuoli, E., Meckler, A.N., Ziegler, M., Millan, I.M., Kluge, T., Deak, J., Hanselmann, K., John, C.M., Yan, H., Liu, Z., Bernasconi, S.M., 2015. Temperature dependence of oxygen- and clumped isotope fractionation in carbonates: a study of travertines and tufas in the 6–95 °C temperature range. *Geochim. Cosmochim. Acta* 168, 172–192. <https://doi.org/10.1016/j.gca.2015.06.032>.
- Malagnini, L., Lucente, F.P., De Gori, P., Akinci, A., Munafò, I., 2012. Control of pore fluid pressure diffusion on fault failure mode: insights from the 2009 L'Aquila seismic sequence. *J. Geophys. Res.* 117. <https://doi.org/10.1029/2011JB008911>.
- Martelli, M., Nuccio, P.M., Stuart, F.M., Burgess, R., Ellam, R.M., Italiano, F., 2004. Helium-strontium isotope constraints on mantle evolution beneath the Roman comagmatic province, Italy. *Earth Planet. Sci. Lett.* 224, 295–308.
- McArthur, J., Howarth, R., Bailey, T., 2001. Strontium isotope stratigraphy: LOWESS version 3: best fit to the marine Sr-isotope curve for 0–509 Ma and accompanying look-up table for deriving numerical age. *J. Geol.* 109, 155–170.
- Menzies, C.D., Teagle, D.A., Crav, D., Cox, S.C., Boyce, A.J., Barrie, C.D., Roberts, S., 2014. Incursion of meteoric waters into the ductile regime in an active orogen. *Earth Planet. Sci. Lett.* 399, 1–13. <https://doi.org/10.1016/j.epsl.2014.04.046>.
- Miller, S.A., Collettini, C., Chiaraluce, L., Cocco, M., Barchi, M., Kaus, B.J.P., 2004. Aftershocks driven by a high-pressure CO₂ source at depth. *Nature* 427, 724–727. <https://doi.org/10.1038/nature02251>.
- Minissale, A., 2004. Origin, transport and discharge of CO₂ in central Italy. *Earth-Sci. Rev.* 66, 89–141. <https://doi.org/10.1016/j.earscirev.2003.09.001>.
- Montone, P., Salvini, F., 1992. Geologia strutturale dei rilievi tra Colli di Monte Bove (Carsoli) e Tagliacozzo, Abruzzo. *Geol. Rom.* 29, 15–23.
- Mostardini, F., Merlini, S., 1986. Appennino centro meridionale, sezioni geologiche e proposta di modello strutturale. *Mem. Soc. Geol. Ital.* 35, 177–202.
- O'Neil, J.R., Clayton, R.N., Mayeda, T.K., 1969. Oxygen isotope fractionation in divalent metal carbonates. *J. Chem. Phys.* 51, 5547–5558.
- Petitta, M., Mastorillo, L., Preziosi, E., Banzato, F., Barberio, M.D., Billi, A., Cambi, C., De Luca, G., Di Carlo, P., Di Curzio, D., Di Salvo, C., Nanni, T., Palpacelli, S., Rusi, S., Saroli, M., Tallini, M., Tazioli, A., Valigi, D., Vivalda, P., Doglioni, C., 2018. Watertable and discharge changes associated with the 2016–2017 seismic sequence in central Italy: hydrogeological data and a conceptual model for fractured carbonate aquifers. *Hydrogeol. J.* <https://doi.org/10.1007/s10040-017-1717-7>.
- Ramsay, J.G., 1980. The crack-seal mechanism of rock deformation. *Nature* 284, 135–139.
- Roberts, G.P., Michetti, A.M., 2004. Spatial and temporal variations in growth rates along active normal fault systems: an example from the Lazio-Abruzzo Apennines, central Italy. *J. Struct. Geol.* 26, 339–376. [https://doi.org/10.1016/S0191-8141\(03\)00103-2](https://doi.org/10.1016/S0191-8141(03)00103-2).
- Sibson, R.H., 1993. Load-strengthening versus load-weakening faulting. *J. Struct. Geol.* 15, 123–128. [https://doi.org/10.1016/0191-8141\(93\)90090-W](https://doi.org/10.1016/0191-8141(93)90090-W).
- Sibson, R.H., 2000. Fluid involvement in normal faulting. *J. Geodyn.* 29, 469–499. [https://doi.org/10.1016/S0264-3707\(99\)00042-3](https://doi.org/10.1016/S0264-3707(99)00042-3).
- Smeraglia, L., Berra, F., Billi, A., Boschi, C., Carminati, E., Doglioni, C., 2016. Origin and role of fluids involved in the seismic cycle of extensional faults in carbonate rocks. *Earth Planet. Sci. Lett.* 450, 292–305. <https://doi.org/10.1016/j.epsl.2016.06.042>.
- Stewart, I.S., Hancock, P.L., 1990. Brecciation and fracturing within neotectonic normal fault zones in the Aegean region. *Geol. Soc. (Lond.) Spec. Publ.* 54, 105–110. <https://doi.org/10.1144/GSL.SP.1990.054.01.11>.
- Ünal-Imer', E., Uysal, I.T., Zhao, J.X., Is, I., k V., Shulmeister, J., Imer, A., Feng, Y.X., 2016. CO₂ outburst events in relation to seismicity: constraints from microscale geochronology, geochemistry of late Quaternary vein carbonates, SW Turkey. *Geochim. Cosmochim. Acta* 187, 21–40. <https://doi.org/10.1016/j.gca.2016.05.006>.
- Uysal, I.T., Feng, Y.X., Zhao, J.X., Bolhar, R., Is, ik, V., Baublys, K.A., Yago, A., Golding, S.D., 2011. Seismic cycles recorded in late Quaternary calcite veins: geochronological, geochemical and microstructural evidence. *Earth Planet. Sci. Lett.* 303, 84–96. <https://doi.org/10.1016/j.epsl.2010.12.039>.
- Veizer, J., 1983. Trace elements and isotopes in sedimentary carbonates. In: Reeder, R.J. (Ed.), *Carbonates: Mineralogy and Chemistry*. In: *Review in Mineralogy*. Mineralogical Society of America, Washington, D.C., pp. 265–300.
- Valoroso, L., Chiaraluce, L., Piccinini, D., Di Stefano, R., Schaff, D., Waldhauser, F., 2013. Radiography of a normal fault system by 64,000 high-precision earthquake locations: the 2009 L'Aquila (central Italy) case study. *J. Geophys. Res.* 118, 1156–1176. <https://doi.org/10.1002/jgrb.50130>.
- Williams, R.T., Goodwin, L.B., Sharp, W.D., Mozley, P.S., 2017. Reading a 400,000-year record of earthquake frequency for an intraplate fault. *Proc. Natl. Acad. Sci.* 114, 4893–4898. <https://doi.org/10.1073/pnas.1617945114>.